Surveys in Geophysics
https://doi.org/10.1007/s10712-024-09845-9

Investigation of Fluid Types in Shale Oil Reservoirs

Xiaojiao Pang[1,2,3] · Guiwen Wang[1,2] · Lichun Kuang[1,2] · Jin Lai[1,2] · Nigel P. Mountney[3]

Received: 8 November 2023 / Accepted: 8 May 2024

Abstract
Lacustrine shale oil resources are essential for the maintenance of energy supply. Fluid types and contents play important roles in estimating resource potential and oil recovery from organic-rich shales. Precise identification of fluid types hosted in shale oil reservoir successions that are characterized by marked lithological heterogeneity from only a single well is a significant challenge. Although previous research has proposed a large number of methods for determining both porosity and fluid saturation, many can only be applied in limited situations, and several have limited accuracy. In this study, an advanced logging technique, combinable magnetic resonance logging (CMR-NG), is used to evaluate fluid types. Two-dimensional nuclear magnetic resonance (2D-NMR) experiments on reservoir rocks subject to different conditions (as received, after being dried at 105 ℃, and kerosene imbibed) were carried out to define the fluid types and classification criteria. Then, with the corresponding Rock–Eval pyrolysis parameters and various mineral contents from X-ray diffraction, the contribution of organic matter and mineral compositions was investigated. Subsequently, the content of different fluid types is calculated by CMR-NG (combinable magnetic resonance logging, viz. 2D NMR logging). According to the fluid classification criteria under experimental conditions and the production data, the most favorable model and optimal solution for logging evaluation was selected. Finally, fluid saturations of the Cretaceous Qingshankou Formation in the Gulong Sag were calculated for a single well. Results show that six fluid types (kerogen-bitumen-group OH, irreducible oil, movable oil, clay-bound water, irreducible water, and movable water) can be recognized through the applied 2D NMR test. The kerogen-bitumen-group OH was mostly affected by pyrolysis hydrocarbon (S_2) and irreducible oil by soluble hydrocarbon (S_1). However, kerogen-bitumen-group OH and clay-bound water cannot be detected by CMR-NG due to the effects of underground environmental conditions on the instruments. Strata Q8–Q9 of the Qing 2 member of the cretaceous Qingshankou Formation are the most favorable layers of shale oil. This research provides insights into the factors controlling fluid types and contents; it provides guidance in the exploration and development of unconventional resources, for example, for geothermal and carbon capture, utilization, and storage reservoirs.

Keywords Fluid identification · Shale oil · 2D NMR tests · CMR-NG · Controlling factors

Extended author information available on the last page of the article

Published online: 22 June 2024

Article Highlights

- Fluid types underground are identified by 2D NMR experiments and CMR-NG logs
- A map showing the difference between the longitudinal relaxation time and the transverse relaxation time, termed the T_1–T_2 map, is used to unravel the fluid occurrence and content
- Fluids corresponding with short T_1–T_2 relaxation times are mostly affected by pyrolytic components rather than mineral components

1 Introduction

Unconventional resources make up a substantial part of global oil and gas exploration, development and production. Reservoirs in relatively low permeability and low porosity rocks (so-called tight and shale reservoirs) that host shale oil and gas are important targets and assets for energy companies (EIA 2023; Fang et al. 2019; Li et al. 2019). Existing unconventional reservoirs are mainly distributed in North America, followed by Eastern Europe and Asia (EIA 2023; Fang et al. 2019). There are more than 100 petroliferous basins all over the world (EIA 2023; Fang et al. 2019). Of these, the largest shale oil enrichment basin is the West Sibrian Basin in Russia, accounting for 16.5% of the global shale oil resources. The second and third largest are the Permian Basin and Western Gulf Mexico Basin of the United States, respectively. The Junggar and Songliao Basins of China rank 10th and 11th, respectively (Fang et al. 2019). The Gulong shale located in the Gulong Sag of the central depression of the Songliao Basin is the focus of this study due to its favorable resource potential.

The shale oil reservoir of the Qingshankou Formation, in the Gulong Sag, Songliao Basin is characterized by high clay content, diverse mineral composition, pronounced lamination within many beds, and strong lithological heterogeneity and anisotropy. It is important to accurately evaluate the shale oil saturation parameters in reservoir assessment and evaluation. Previous studies have introduced numerous methods with which to calculate resource potential parameters (Ballinas et al. 2023; Li et al. 2023; Zhao et al. 2023). The traditional saturation calculation method is the Archie Formula or advanced Archie Formula (Han et al. 2019; Li et al. 2022; Zhu et al. 2023). However, these methods are not suitable for the Gulong Shale due to the complex pore structure and the presence of micro- and nano-scale pores, for which electrical experiments to determine porosity and saturation are not suitable. In addition, conventional well-log suites—for example, resistivity logs, gamma ray logs, and three porosity logs—are not able to detect the variation of the reservoir space, fluid properties, and lithology clearly. Nuclear Magnetic Resonance (NMR) has developed as a commonly applied technique to evaluate physical properties (porosity, permeability, and pore distribution) qualitatively and quantitatively both in well-log and core experiments (Liu et al. 2022; Ramia and Martin 2016). For one-dimensional NMR, only transverse relaxation time (T_2) can be detected, but this is insufficient to separate different fluid types, because of the overlapping of different fluid T_2 signals (Zhang et al. 2020; Mukhametdinova et al. 2021). For saturation calculation using the NMR test, centrifugation measurements required to obtain the oil saturation of samples are necessary for the calibration of the NMR logs (Liu et al. 2019). However, centrifugation tests are difficult to conduct in reservoirs characterized by lamination and lamellation fractures. Thus, a new method to estimate the oil content and saturation, and fluid types is urgently required.

Compared with one-dimensional NMR technology, two-dimensional NMR (2D NMR) technology can simultaneously detect and record more parameters, such as transverse

relaxation time T_2, longitudinal relaxation time T_1, diffusion coefficient D, and internal magnetic field gradient G. This improves the accuracy of fluid type identification and fluid saturation calculation (Khatibi et al. 2019; Yan et al. 2021). This technique is now widely used in the evaluation of physical properties, oil saturation, and mobility of unconventional oil and gas reservoirs (Qin et al. 2022). Additionally, 2D NMR can also be used to elucidate wettability (Liang et al. 2019). However, to detect the 2D NMR signal characteristics and condition of in-situ preserved rocks, there are very specific requirements for how core samples must be obtained. Moreover, the 2D NMR experiment is costly and the length and quantity of cores that can be measured are limited. To make up for these shortcomings, 2D NMR logs (CMR-NG) are usually applied to measure and record the 2D NMR signal from only a single well.

The aim of this study is present a workflow for the application of 2D NMR as the key technique to determine the saturation and proportion of solid organics, water, and oil behaviors in shales of the Qingshankou Formation, Gulong Sag, Songliao Basin, China. Specific research objectives are as follows: (1) to divide the fluid types in shales and determine the classification criteria according to T_1–T_2; (2) to elucidate factors controlling various fluid types; (3) to evaluate the oil potential of different layers of the Qingshankou Formation using 2D NMR logs.

2 Geological Setting

As a well-known petroliferous basin located in northeastern China, the Songliao Basin is present in the Heilongjiang, Jilin, and Liaoning provinces of China; the basin covers are area of $\sim 26 \times 10^4$ km^2, with a length of 820 km (north–south) and a width of 350 km (east–west) (Fig. 1A). During its evolution, the basin experienced four major structural episodes: upper mantle uplift in the Middle-Late Jurassic; continental rifting from the late Jurassic to Early Cretaceous; rapid subsidence (the so-called depression stage) in the late Cretaceous; and inversion from late Cretaceous to the Quaternary (Ge et al. 2010; Wang et al. 2022). The structure of the Songliao Basin is characterized by seven tectonic zones: the Central Depression, Northern Plunge, Western Slope, Southwestern Uplift, Kailu Depression, Southeastern Uplift, and Northeastern Uplift (Fig. 1B). The Central Depression can be further divided into 11 secondary tectonic units and the Gulong Sag is one of these (Fig. 1C). The Gulong Sag is bounded by the Honggang terrace to the northwest, the Qijia Sag to the north, the Changling Sag to the south, and the Daqing Placanticline to the east (Fig. 1C). Within the Gulong Sag, three formations accumulated during the episode of active faulting: the Huoshiling, Shahezi, and Yingcheng formations (Ge et al. 2010; Cheng 2019; Wang et al. 2022). Active volcanism occurred during the emplacement of both the Huoshiling and Yingcheng formations (Cheng 2019; Wang et al. 2022). Five formations accumulated during the depression stage: the Kuloudeng, Quantou, Qingshankou, Yaojia, and Nenjiang formations (Ge et al. 2010; Wang et al. 2021; Pang et al. 2023a, b). Of these, the Qingshankou Formation became a focus of hydrocarbon production due to its medium–high thermal maturity of organic matter (Liu et al. 2018, 2019, 2020). A counter map of vitrinite reflectance and the locations of key wells are shown in Fig. 1D. The Qingshankou Formation was characterized by semi-deep to deep lacustrine depositional environment and experienced a major transgression (Liu et al. 2019, 2020). The lithofacies are dominated by laminated siliceous shales and laminated clay shales interbedded with siltstones, shelly limestones, and massive dolomite, implying a depositional environment that was

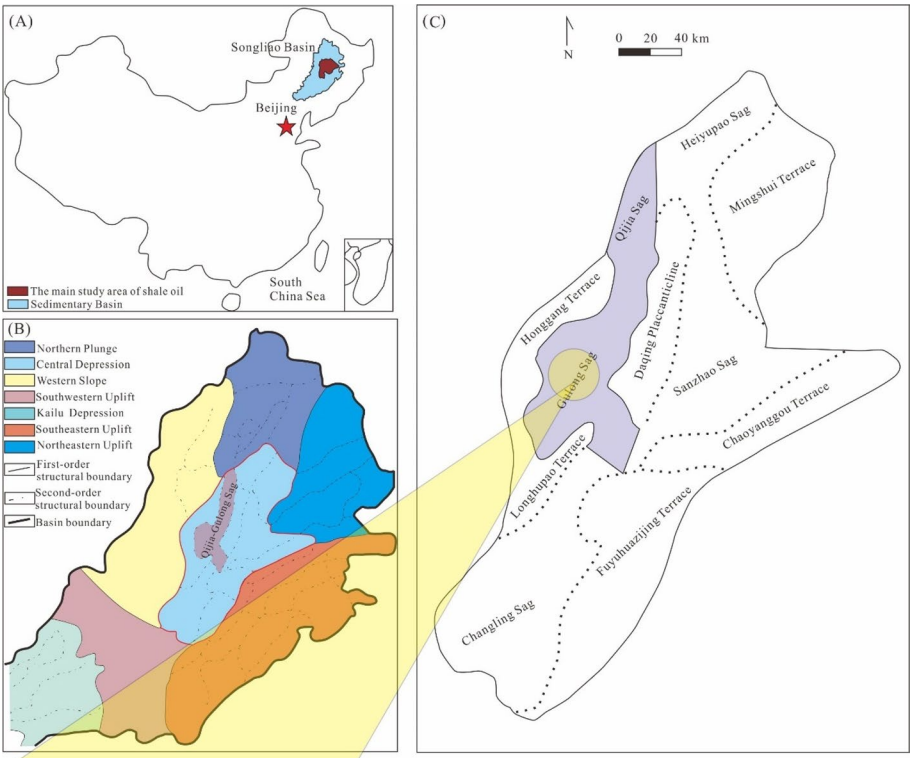

(E)

Strata the top depth (m)			Well 1	Well 2HC	Well 8HC	Well SY1	Well SY2	Well SY3	Well A34	Well 7
K,qn	K,qn$_3$	Q9	2397.57	2227.04	2373.80	2307.96	2049.43	1948.81	2131.85	2399.80
		Q8	2418.90	2251.74	2395.40	2324.89	2066.08	1960.90	2153.09	2430.00
		Q7	2436.67	2270.57	2412.60	2341.75	2080.59	1972.14	2170.47	2450.00
	K,qn$_2$	Q6	2455.85	2290.41	2428.00	2363.26	2096.97	1981.37	2188.78	2471.43
		Q5	2470.44	2307.55	2444.60	2380.72	2106.64	1995.50	2206.77	2488.40
		Q4	2480.96	2321.78	2458.40	2392.65	2114.22	2009.23	2222.81	2499.83
		Q3	2493.37	2334.84	2470.11	2407.74	2122.76	2021.74	2236.44	2514.41
		Q2	2506.85	2350.02	2483.40	2420.68	2133.23	2033.87	2251.87	2528.60
		Q1	2518.62	2361.49	2495.60	2432.33	2142.05	2043.77	2263.27	2541.40
K,q			2586.69	2377.00	2533.27	2448.50	2154.37	2061.03	2278.70	2558.60

Fig. 1 The location map of the Songliao Basin (**A**), structural zones in the Songliao Basin (**B**), study area (**C**), locations of key wells (**D**), and the stratification data of the key wells in the Qingshankou Formation, Gulong Sag (**E**) (Liu et al. 2019; He et al. 2022)

subject to several transgressive and regressive cycles (Liu et al. 2019). The Cretaceous Qingshankou Formation is divided into three members, form bottom to top, the first member (K_{2qn1}), second member (K_{2qn2}), and third member (K_{2qn3}). The first member and the lowermost part of the second member have been a focus of hydrocarbon exploration and development because they exhibit high total organic carbon (TOC) (Liu et al. 2019; Pang et al. 2023a, b). According to the Gamma-Ray log data, the first member and the lowermost part of the second member are further subdivided into nine stratal units (Fig. 1E).

3 Samples and Methods

Core, scanning electron microscope (SEM), thin section, and X-ray diffraction (XRD) were used to analyze the petrology characteristics of the reservoir. Rock–Eval pyrolysis analysis was carried out on 16 samples from four key Wells (Well SY1, Well SY2, Well SY3, and Well A34) using the OGE-VI oil and gas evaluation workstation (Table 1). Then, pyrolysis properties including soluble hydrocarbon (S_1), pyrolysis hydrocarbon (S_2), organic carbon dioxide (S_3), residual carbon (S_4), total organic carbon (TOC), hydrogen index (I_H), oxygen index (I_O), total hydrocarbon (S_1+S_2 or Pg), and the maximum temperature of the pyrolysis peak (T_{max}) were obtained. S_1 was tested at 300 ℃ for 3 min to provide an indication of the quantity of free petroleum present in the sample. S_2 was measured by increasing the temperature from 300 to 550 ℃ to provide an indication of the kerogen content present in the sample at the time of analysis. S_3 was determined as the yield of carbon dioxide during the pyrolysis of kerogen. S_4 was tested after 600 ℃. T_{max} was determined as the maximum temperature corresponding to the highest peak of S_2 pyrolysis peak. I_H and I_O are expressed as $S_2/TOC\times100$ and $S_3/TOC\times100$, respectively.

A total of nine samples from two key wells (Well SY2 and Well SY3) were used for the 2D NMR test. Compared with the low magnetic field, when the hydrogen protons are tested under a high external magnetic field, the fluid signal in the T_1–T_2 map will shift to the left. Under a higher-frequency magnetic field, the magnetic field gradient increases, resulting in a shorter transverse relaxation time, a longer longitudinal relaxation time, and then a larger value of T_1/T_2. Due to the different properties of each fluid type—notably diffusion coefficient, viscosity, and magnetic susceptibility at the solid–liquid interface—the magnetic field strength has different effects on the relaxation time of each type. Taking oil and water as an example, when the magnetic field frequency increases, the transverse relaxation time of oil becomes shorter and more than the water signal, and the longitudinal relaxation time becomes longer and greater than that of the water signal (Qin et al. 2021, 2022). For unconventional oil and gas reservoir analysis, 21 MHz is mostly used in the NMR experiment. Under this circumstance, high-quality echo data can be obtained (Li et al. 2018; Liu et al. 2022). Therefore, the oil and water signals can be separated more specifically. However, experimental data obtained from NMR testing under a 21 MHz magnetic field cannot be directly used to calibrate the NMR logs, because the NMR log detects T_1–T_2 signals under a lower magnetic field, commonly of 2 MHz. For improved NMR log calibration, a 2D NMR test under a low magnetic field (2 MHz) is carried out in this study. It should be noted that there is a problem of overlapping of different components attributed to the low magnetic field intensity. The identification accuracy of different fluid types is not sufficient. The samples are tested under three different conditions: (1) as received (AS), (2) after being dried at 105 ℃ (D), and (3) kerosene imbibed (KI). The laboratory conditions were at normal temperature and atmospheric pressure. The samples were dried, then wrapped with plastic to prevent moisture in the air from affecting the measurement results, and then placed at normal temperature for measurement.

Schlumberger's combinable magnetic resonance logging tool named CMR-MagniPHI (CMR-NG) was used to detect the multiple CPMG echo signals with different waiting times (T_W) in the borehole. Then, multi-echo series joint inversion is processed to obtain a T_1–T_2 map. The original measurement data of CMR-NG mainly include six sets of orthogonal echo channel data. Echo data of each group are stored in order from long to short length of *T*w. Therefore, echo data of different T_W can be extracted according to the number of echoes. The echo data processing of multi-T_W CPMG signals mostly adopts the echo

Table 1 Pyrolysis experimental data for shales in the Qingshankou Formation, Gulong Sag, Songliao Basin

Wells	Samples	Strata	Depth (m)	Length (cm)	T_{max}(℃)	S_1 (mg/g)	S_2 (mg/g)	S_1+S_2 (mg/g)	S_3 (mg/g)	S_4 (mg/g)	TOC (%)	I_H (mg/g)	I_O (mg/g)
Well SY2	C1	K_{2qn1}	2150.65	9	420	5.81	8.23	14.04	0.57	9.52	2.12	388.70	26.92
Well SY2	C2	K_{2qn1}	2142.15	8	413	7.67	7.75	15.42	0.51	6.31	1.91	405.58	26.69
Well SY2	C3	K_{2qn1}	2134.39	11	448	10.46	19.77	30.23	0.68	11.95	3.70	533.73	18.36
Well SY2	C4	K_{2qn1}	2132.64	9	447	4.95	4.90	9.85	0.74	5.47	1.36	359.09	54.23
Well SY2	C5	K_{2qn1}	2126.89	8	440	7.96	11.71	19.67	0.51	5.96	2.23	525.44	22.88
Well SY2	C6	K_{2qn1}	2115.39	8	447	7.00	13.09	20.09	0.77	7.21	2.39	548.05	32.24
Well SY2	C7	K_{2qn1}	2100.39	9	428	1.25	2.33	3.58	0.87	3.45	0.64	362.85	135.48
Well SY2	C8	K_{2qn1}	2106.09	12	445	4.13	8.98	13.11	0.71	9.87	2.08	432.74	34.21
Well SY2	C9	K_{2qn1}	2088.09	7.5	444	10.51	21.38	31.89	0.88	4.32	3.08	694.41	28.58
Well SY3	D1	K_{2qn1}	2034.88	5	453	6.61	70.90	77.51	0.53	2.41	6.67	1062.28	7.94
Well SY3	D2	K_{2qn1}	2036.42	5	445	15.15	77.79	92.94	0.82	1.56	7.87	988.43	10.42
Well SY3	D3	K_{2qn1}	2036.72	5	447	7.25	34.22	41.47	0.74	5.63	4.01	854.43	18.48
Well SY1	E1	K_{2qn1}	2436.53	9	446	8.20	8.62	16.82	0.48	6.77	2.07	415.81	23.15
Well A34	F1	K_{2qn1}	2253.71	6	442	6.40	4.58	10.98	0.41	40.80	4.99	91.76	8.21
Well A34	F2	K_{2qn1}	2254.28	7	436	5.52	6.94	12.46	0.90	15.63	2.60	267.21	34.65
Well A34	F3	K_{2qn1}	2257.13	5	443	4.58	4.87	9.45	0.78	39.63	4.75	102.58	16.43

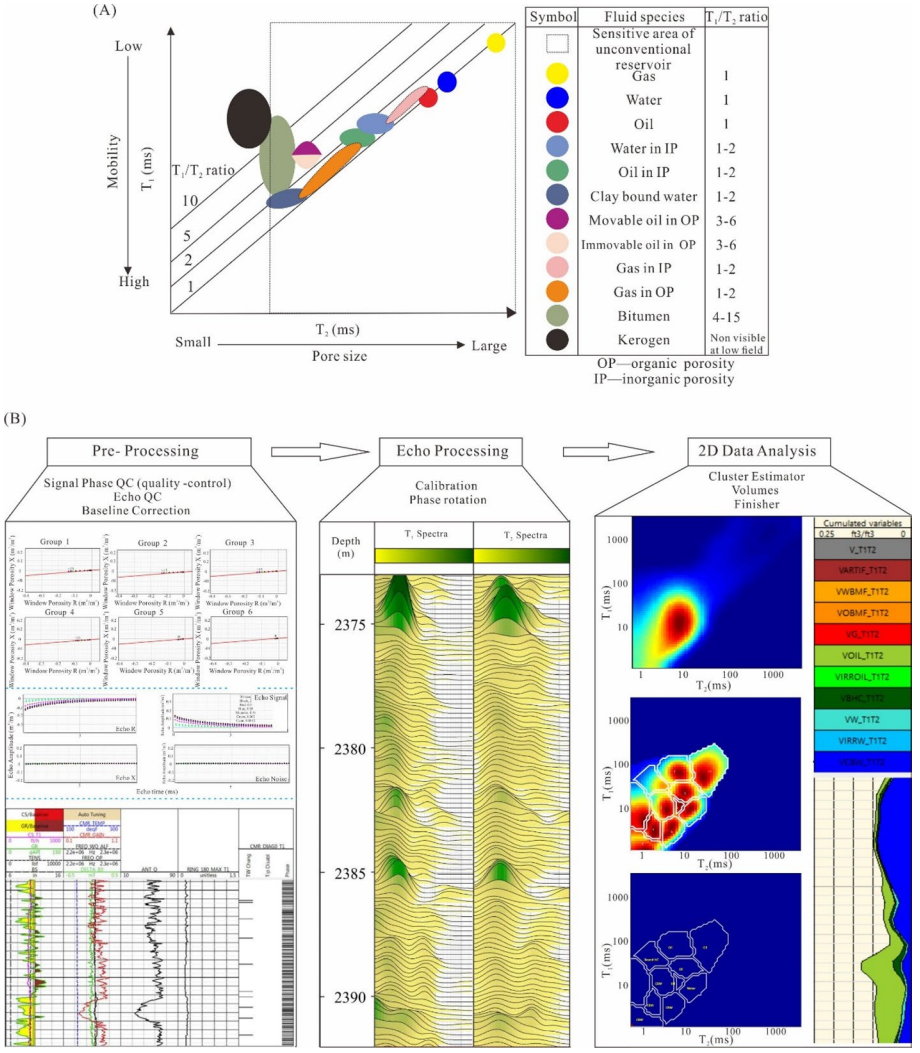

Fig. 2 Location of hydrogen-bearing components of shale on T_1–T_2 map (**A**) and workflow of fluid interpretation by CMR-NG (**B**). Modified from Li et al. 2018; help center of Schlumberger

series inversion method (Guo et al. 2019; Yarman and Mitchell 2019), which is processed by Techlog2019 advanced interpretation module. CMR-NG analysis consists of three steps: cluster estimator, volumes, and finisher (Fig. 2).

The resonant frequency of the above 2D NMR experimental conditions is 2 MHz, which is consistent with the magnetic field of the CMR-NG instrument. Therefore, the experimental data can be used to calibrate the CMR-NG logging. Thus, the standard of fluid type classification under experimental conditions can be applied to logging. However, in the actual logging process, due to the requirements of the instrument's data acquisition method and aging, it is difficult to achieve the same effect as that of experimental measurement. Moreover, the experimental measurement is not entirely representative of the natural

state of underground rock nuclear magnetic response characteristics, so there will be some deviation between these two.

In this study, first, the classification criteria of different fluid types were established according to the energy cluster variation of T_1–T_2 maps under three conditions (as received, after being dried at 105 ℃, and kerosene imbibed). Then the content of various fluid types can be calculated through T_1–T_2 data obtained by 2 MHz 2D NMR experiment. Subsequently, combing the mineral composition, lithology, and pyrolysis parameters, the controlling factors of different fluids were discussed. Consequently, logging evaluation of oil saturation in the Qingshankou Formation in a single well was unraveled using CMR-NG (2 MHz 2D NMR log).

4 Results

4.1 Rock Characteristics

4.1.1 Mineral Composition and Pore Space

The reservoir is highly heterogeneous with complex sedimentary components. According to the observation of the SEM, the dominant minerals are quartz, feldspar (albite and orthoclase), clay (mainly illite, mixed layer illite/smectite, and chlorite), ankerite, calcite, and pyrite (Fig. 3). Compared with other shale oil and gas reservoirs, for example the Barnett shale in the Fort Worth Basin in the United States, the content of clay minerals is higher and the content of carbonates is lower in the Qingshankou Formation. The SEM images show that the illite is characterized by layered structure, contributing to the development lamellation fractures and beddings under the compaction in the burial history.

As an unconventional oil reservoir, the succession studied here is characterized by relatively low porosity with an average value of 7.7% and low permeability (horizontal permeability lower than 0.61×10^{-3} μm^2 and vertical permeability lower than 0.056×10^{-3} μm^2 (Gao et al. 2022). The SEM images indicate that the pore types of the Qingshankou Formation can be divided into organic pores and inorganic pores. The inorganic pores can be further classified into dissolution pores and intercrystalline pores (Fig. 4). Additionally, natural fractures, and microfractures can be observed from cores and thin sections. The radius of pores mainly ranges from 2 to 50 nm (mesopores) (Liu et al. 2018; Bai et al. 2022). Lamellation fractures played an important role in oil migration and accumulation and provided the majority of the reservoir space (Zhang et al. 2021; He et al. 2022; Pang et al. 2023a, b).

4.1.2 Geochemical Characteristics

Parameters commonly used to evaluate the abundance of organic matter include total organic carbon (TOC), chloroform asphalt "A" and total hydrocarbon (HC), as well as hydrocarbon generation potential (Pg) obtained from rock pyrolysis experiment. Total organic carbon (TOC) is an important index to evaluate the abundance of organic matter. It is worth noting that in the process of hydrocarbon generation by the evolution of organic matter, with the increase of maturity, part of the oil and gas migrated to the reservoir, causing part of the carbon to discharge from the source rock. Therefore, it is important to restore the original total organic carbon (both residual and discharged

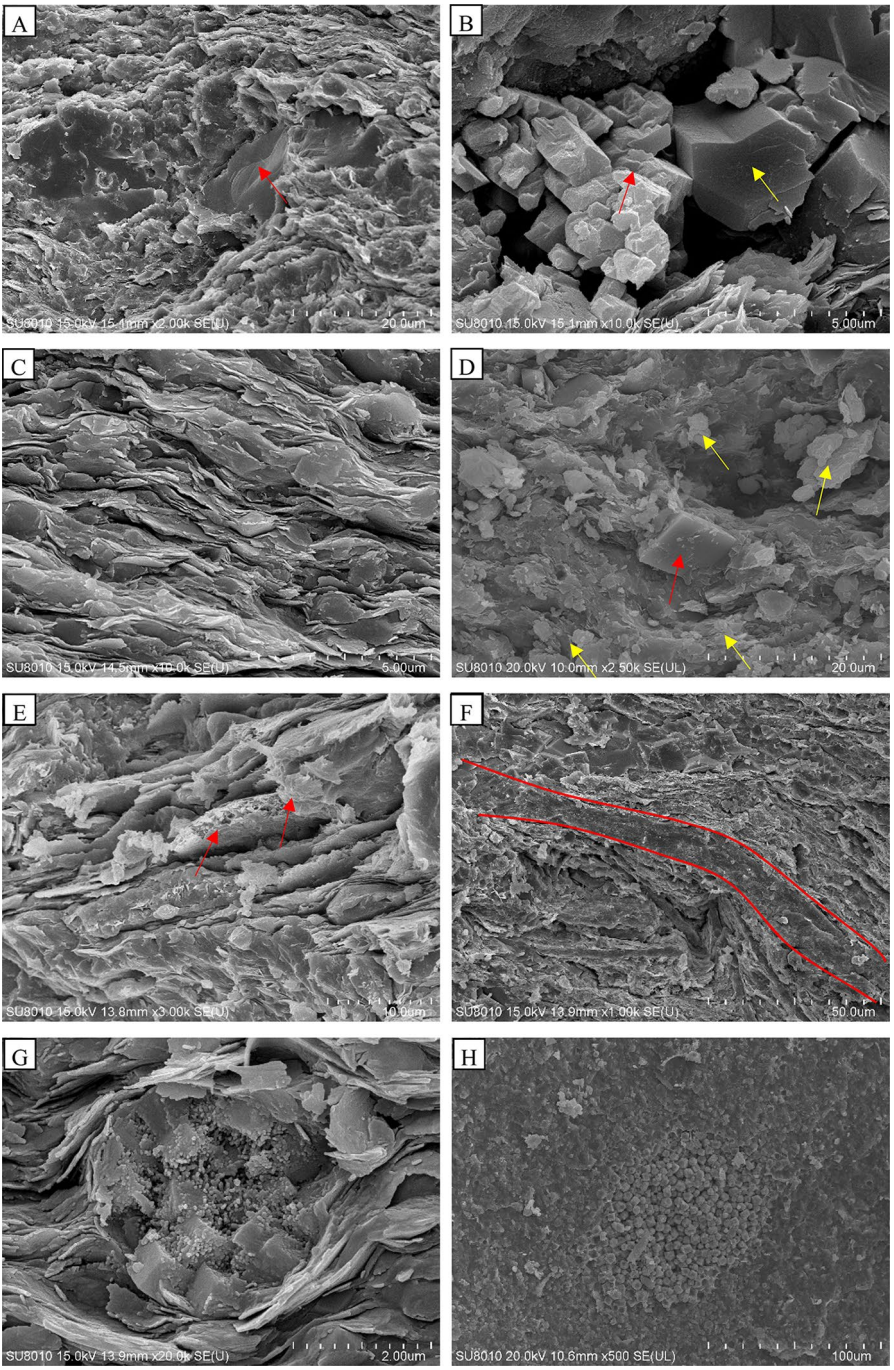

Fig. 3 The characteristics of petrology in the Qingshankou Formation, Gulong Sag, Songliao Basin. **A** Quartz, Well 2HC, 2322.72 m. **B** Albite and orthoclase, Well 2HC, 2372.05 m. **C** Layered illite, Well 2HC, 2322.72 m. **D** Clay minerals (yellow arrow), dolomite (red arrow), Well 2HC, 2247.2 m. **E** Mixed layer illite/smectite, Well 2HC, 2322.72m. **F** Shell, Well 2HC, 2319.43 m. **G** Pyrite, Well 2HC, 2319.43 m. **H** Pyrite, Well 2HC, 2325.14 m.

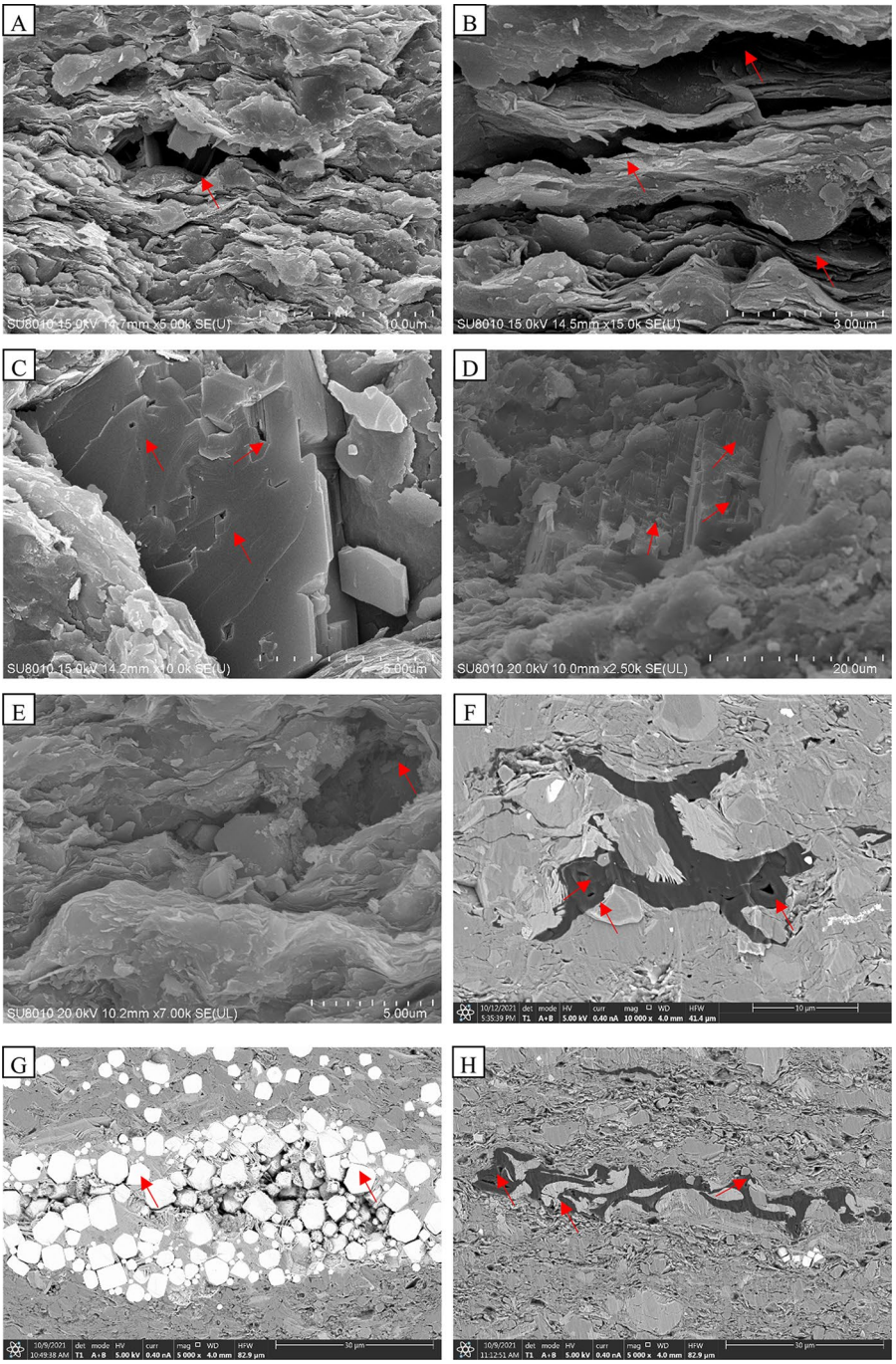

Fig. 4 Types and features of lithology in the Qingshankou Formation, Gulong Sag, Songliao Basin. **A** Clay intercrystalline pores, Well 2HC, 2333.9 m. **B** Interlayer fractures, Well 2HC, 2322.72 m. **C** Intraparticle dissolution pores in orthoclase, Well 2HC, 2333.9 m. **D** Intraparticle dissolution in anorthose, Well 2HC, 2245.3 m. **E** Dissolution pores along the particle edge, Well 2HC, 2247.2 m. **F** Organic matter pores, Well 8HC, 2449.1 m. **G** Intercrystalline pores in pyrite, Well 8HC, 2511.1 m. **H** Organic matter pores (fractures), Well 8HC, 2511.1 m.

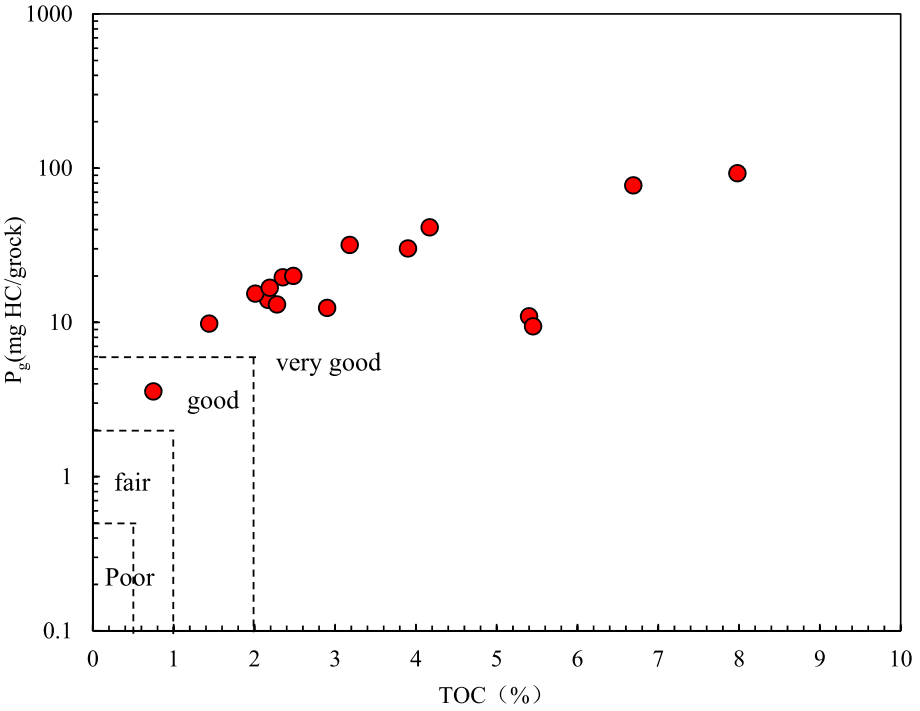

Fig. 5 Crossplot of TOC and Pg in the Qingshankou Formation, Gulong Sag, Songliao Basin

organic carbon) prior to an assessment of the source rock. No migration is recognized in the Qingshankou Formation of the Gulong Sag (Feng et al. 2020). Shales with TOC contents of less than 0.5%, 0.5–1%, 1–2%, and greater than 2% represent poor, fair, good, and excellent petroleum potential, respectively (Peters and Cassa 1994; Hu et al. 2021). Meanwhile, Pg with values of less than 0.2 mg HC/g rock, 0.2 mg HC/g rock–2 mg HC/g rock, 2 mg HC/g rock–6 mg HC/g rock, and greater than 6 mg HC/g rock represent poor, fair, good, and excellent source rocks, respectively. The organic carbon content ranges from 0.75 to 7.98%, with an average value of 3.46%. The crossplot of the TOC and Pg shows that most core data are located in the favorable area, indicating the shale of the Qingshankou Formation is a high-quality source rock (Fig. 5).

According to the pyrolysis analysis of the rocks, the parameters of hydrogen index (I_H), oxygen index (I_O), and maximum pyrolysis peak (T_{max}) are used to determine that the organic matter types of Qingshankou Formation in the Gulong Sag. The results show that the kerogen types are mainly Type I and Type II, indicating that the study area is dominated by oil-prone kerogen with an oil generation (Fig. 6). Generally, Type I and Type II are attributed to flourishing low aquatic algae (Liang et al. 2015; Martins et al. 2020). Organic matter is mainly derived from layered alginate and telalginite, which is characterized by high conversion rate of hydrocarbon generation and a large area shrinkage rate. In the process of hydrocarbon generation and expulsion by thermal evolution of organic matter, a large number of nano-sized elongated pores (fractures) appeared along layers, which are defined as lamellation fractures (Feng et al. 2021).

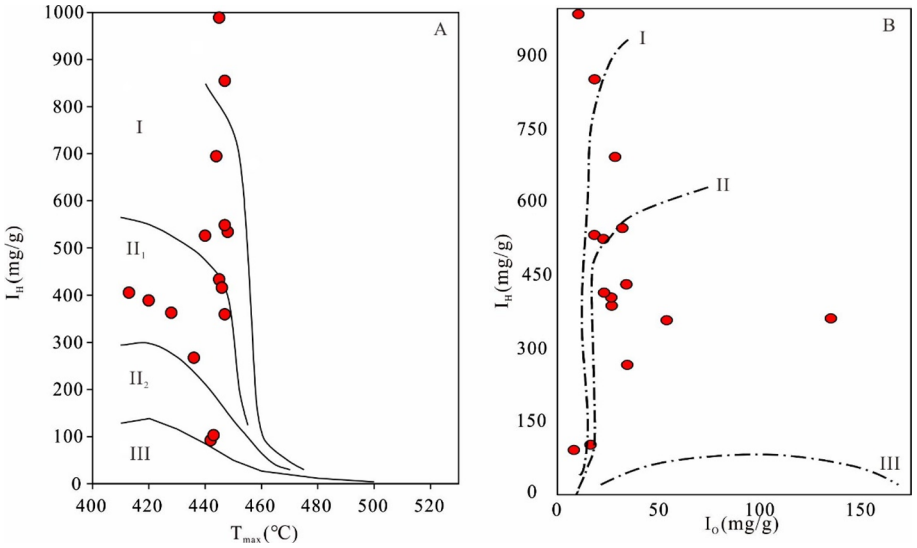

Fig. 6 Organic matter types in the Qingshankou Formation, Gulong Sag, Songliao Basin. Correlations between pyrolysis T_{max} and hydrogen index (I_H) **A** and correlations between I_H and I_O **B**

This type of reservoir space contributed the most storage space and was good a migration pathway.

The reflectivity of vitrinite (*R*o) and T_{max} is commonly used to evaluate thermal maturity. During the thermal evolution of organic matter, a series of reactions such as thermal desorption of alkanes and fusion of aromatic ring occurred, and all that matters is this reaction is irreversible. The pyrolysis process of kerogen has a good consistency with the evolution of vitrinite. With the increase of thermal evolution degree, the reflectivity of vitrinite increases and the transmittance decreases. Therefore, *R*o can be used to evaluate the maturity of organic matter. The pyrolysis experimental results show that the *R*o values of the Qingshankou Formation range from 0.7 to 1.7, with an average value of 1.3. The T_{max} distribution ranges from 413 to 453 ℃ with a mean of 440 ℃ (Table 1), indicating that the shales of the Qingshankou Formation are in medium to high stages of thermal maturity, which is conducive to shale oil enrichment and with broad exploration and development prospects.

4.1.3 Lithology

The lithology of the Qingshankou Formation in the Gulong Sag is identified by polarizing microscope and core observation. It is dominated by shale, which mainly contains felsic shale and clayed shale, shelly limestone and dolomite, and a little siltstone as well (Fig. 7). Among them, the structure of shelly limestone and dolomite are mostly massive, and usually interlayered with other rocks. Clayed shale and felsic shale account for more than 80%, which are favorable lithologies for shale oil formation and enrichment (Liu et al. 2019; Gao et al. 2022; Pang et al. 2023b). Thin section observation displays that four types of minerals can be identified including felsic, clay, carbonate, mixed, and organic matter (Fig. 7A–D). Among them, the content of clay minerals is the highest,

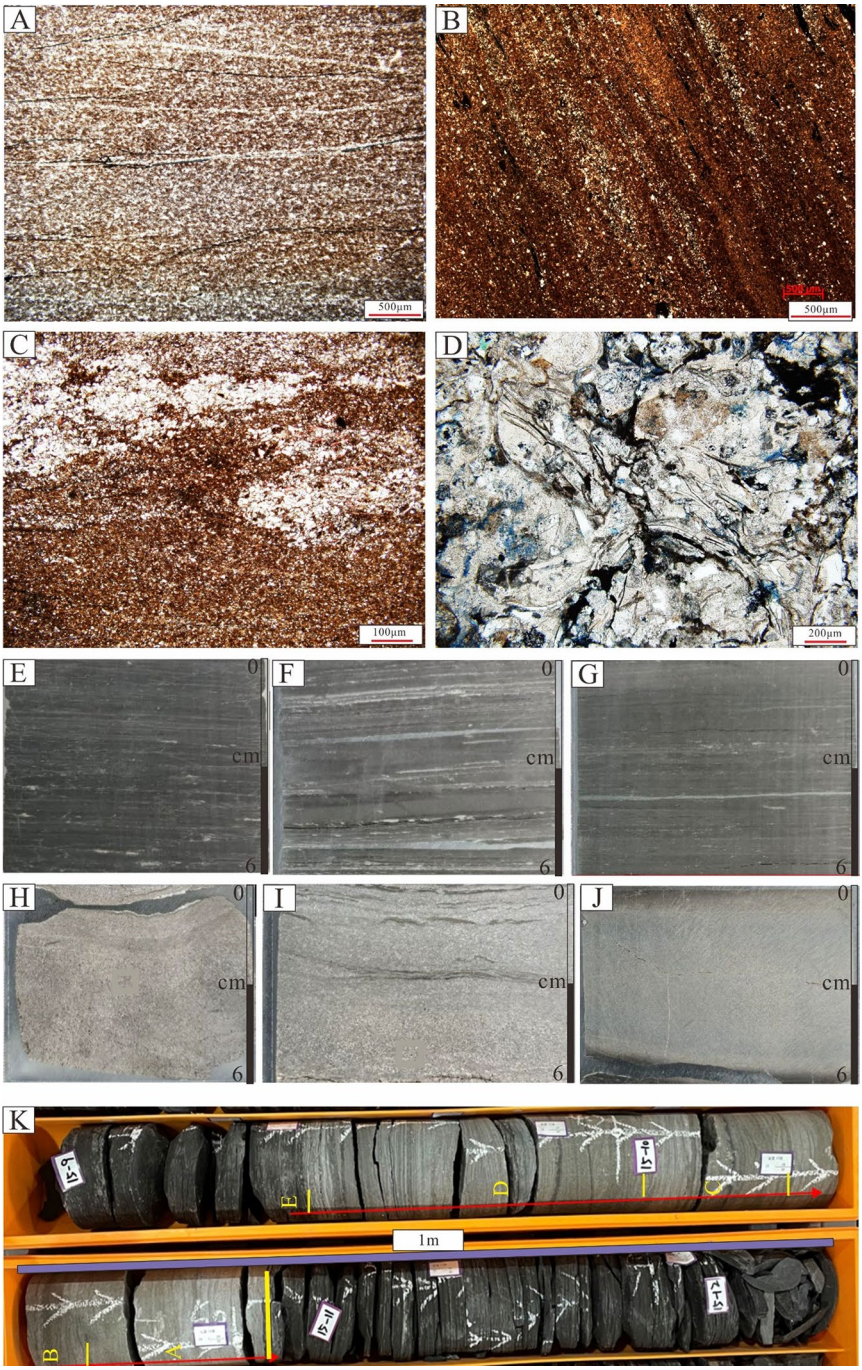

Fig. 7 Types and features of lithology in the Qingshankou Formation, Gulong Sag, Songliao Basin. **A** Felsic shale, Well 2HC, 2325.14 m.**B** Clay shale, Well GY1, 2566.76 m. **C** Felsic shale (upper) and clay-prone shale, Well 2HC, 2247.2 m. **D** Shelley limestone, Well 2HC, 2373.86 m. **E** Clay-prone shale, Well 8HC, 2508.4 m. **F** Felsic shale, Well 8HC, 2491.15 m. **G** Felsic shale, Well 8HC, 2492.49 m. **H** Shelley limestone, Well 8HC, 2489.9 m. **I** Shelley limestone, Well 8HC, 2491.65 m. **J** Dolostone, Well 8HC, 2496.28 m. **K** Bouma sequence, Well 17, 2360 m.

followed by felsic minerals. The content of mixed and organic matter minerals is the lowest.

The felsic shale is distributed in the whole Qingshankou Formation, accounting for 20%. Several lake level decreases increase circles occurred during the deposition of K_{2qn1} resulting in deposition of shale interbedded with fine-grained siltstones (Liu et al. 2019). Conversely, the supply of terrigenous clastic rocks increased. Therefore, the content of felsic minerals increased, and felsic shale increased as well. The core observation shows that this type of rock is grayish black with obvious laminae. Affected by liquefaction, some of the laminae and lamellation are disturbed (Fig. 7F, G). Under the Leica polarizing microscope, most of the detrital grains are grayish brown, quartz and anorthose, which accounts for 70%, and subangular and of high sphericity (Fig. 7A). Calcite and ankerite minerals are rarely observed, and are mostly the products of cementation and metasomatism in the late evolution stage. It can be seen that pyrite in the form of particles or aggregates is distributed among the particles and are mostly associated with clay minerals (Fig. 7A).

Clay-prone shale is widely distributed in the study area, accounting for ~ 65% of the studied succession. The core is grayish black to dark, with laminae and lamellation developed. The boundary between some beddings or laminae is not clear, and it can be seen that a large amount of pyrite is distributed in star-point shape, with the diameter of particles up to 3 mm. Some of them are connected to the laminae laterally, and there are many small calcite veins distributed along the laminae (Fig. 7E). Under the parallel polarized light, the clay-prone shale is characterized by brown, brown-yellow, and black-brown color. The clastic particles are mainly quartz, with a subangular to circular shape, with a particle size less than 0.05 mm, and are mostly distributed among clay minerals in bands (Fig. 7E). The content of carbonate minerals is small, mainly calcite and ankerite. The calcite is filled among the particles as cement, and a small amount of them is distributed along microfractures and lamellation fractures. Ankerite is of good crystal form and scattered among clay minerals in a star-point pattern. The pyrite is mainly granular and aggregates, and some pyrite appeared along the bedding, showing a long black strip under parallel polarized light (Fig. 7B, C).

The shelly limestone facies is less common, accounting for 7% of the studied succession. From the core observation, it is mostly grayish white, with obvious layers of shell debris (Fig. 7H, I). The shell debris mostly comprises fragments of lamellobranchiate organisms, as evident under the optical microscope; biologenic cavities (moulds) are mostly filled with calcite, organic matter or bitumen during diagenesis. Quartz particles are angular to subcircular, distributed unevenly in the matrix, with varying particle sizes up to 0.2 mm (Fig. 7D).

The distribution of dolomite in the study area is similar to that of shelly limestone, and it is apparently less abundant in the Qingshankou Formation, accounting for 8%. The core is gray and characterized by massive structure, with no visible layers (Fig. 7J).

In addition, previous studies have pointed out that in the lacustrine depositional environment of the Qingshankou Formation, various types of gravity flow deposits, including clastic flow and turbidity flow deposits, can be observed (Fu et al. 2014; Du et al. 2015; Liu et al. 2019). However, they are not widespread and mostly occur in the western slope area of the basin (Du et al. 2015). Gravity flow deposits can also be seen in the Qingshankou Formation in the Gulong Sag (Fu et al. 2014; Du et al. 2015) (Fig. 7K). The lithology of these deposits is mainly siltstone, silty mudstone, and mudstone. Controlling factors for gravity flow deposition are complex. Previous studies showed that there was intense volcanic activity during the early stage (Huoshiling and Yingcheng formations) (Cheng 2019;

Wang et al. 2022), and the volcanic eruption processes likely induced earthquakes (Cheng et al. 2019). These earthquakes may have acted as a triggering mechanism for gravity flows in this region (Liu. 2005). These gravity flows carried a large amount of terrigenous debris into the depositional center of the lake. The sedimentary sand bodies of gravity flow origin are thick (~ 1–2 m) with high reservoir quality (Du. 2015; Tang 2015; Zou et al. 2023). Therefore, these deposits types form high-quality reservoir rocks through which oil and gas preferentially migrated, charged, and were preserved after hydrocarbon generation and expulsion from neighboring source rocks. Reservoirs formed of gravity flow deposits are commonly act as sweet spots in unconventional oil and gas exploration (Zou et al. 2023). The turbidity is commonly characterized by low-density and mainly fine silt and clay sediments. The rocks are mainly black shale, dark gray siltstone, and gray fine sandstone, and parallel bedding, horizontal bedding, and cross-bedding are easily observed. The speed of this type of flow is relatively slow and the duration is widely attributed to the weak hydrodynamic energy, and it mostly appears at the tail of a gravity flow activity, forming when rivers flood into lakes (Zhang et al. 2005; Li et al. 2020). Low-density turbidity has typical sedimentary structures and sequences, viz. the Bouma sequence (Li et al. 2020; Zou et al. 2023). In the Qingshankou Formation of the Gulong Sag, a prominent bed preserved with a Bouma-type stratal expression with a deposition thickness of about one meter was found in Well 17 (Fig. 7K). The core photo shows that Section A is mainly composed of sandstone, but no gravel. An obvious erosion interface can be observed at the bottom of sandstone. In Section B, the dominant lithology is siltstone with parallel bedding. Section C is characterized by wavy bedding. Horizontal bedding occurs in sandstone in Section D. On the top of this sequence named Section E, the main lithology is a massive (i.e., internally structureless) mudstone.

4.2 Fluid Types

4.2.1 Classification of Fluids Types via 2D NMR Experiment

The 2D NMR experimental results showed that the six fluid types were identified corresponding to six segments (A, B, C, D, E, and F) divided in the T_1–T_2 map. Region A represented bitumen characterized by T_2 value being less than 1 ms and T_1/T_2 value greater than 10. Region B displayed bound oil in micropores, mainly in organic pores, with T_2 ranging from 1 to 10 ms and T_1/T_2 greater than 3. The movable oil in region C was mainly concentrated in macropores with T_2 greater than 3 and T_1/T_2 greater than 3. Region D was clay-bound water with T_2 value less than 1 ms and T_1/T_2 less than 10. Region E represented immovable water, which was mainly concentrated in small pores, with T_2 ranging from 1 and 10 ms and T_1/T_2 being less than 3. Region F corresponded with movable water, mainly enriched in large inorganic pores, with T_2 values ranging from 10 ms ~ 100 ms and T_1/T_2 less than 3 (Fig. 8, Table 2). Kerogen as an organic matter is characterized by being insoluble in organic solvents. As a mixture of various large molecular organic compounds, the composition of kerogen is complex and not fixed. Bitumen is another type of organic matter that is insoluble in water but soluble in organic solvents. Kerogen cannot be recognized at the low magnetic field (Fleury and Maria. 2016; Silletta et al. 2022). Therefore, region A is mainly bitumen or solid-like organic matter. Under experimental conditions, it is difficult to completely separate clay structural water, bound water and bound oil in micropores, and oil and water in larger pores (Li et al. 2018; Khatibi et al. 2019; Zhang et al. 2020). Therefore, regions B, C, E, and F exhibited overlap. The results of 2D NMR test under

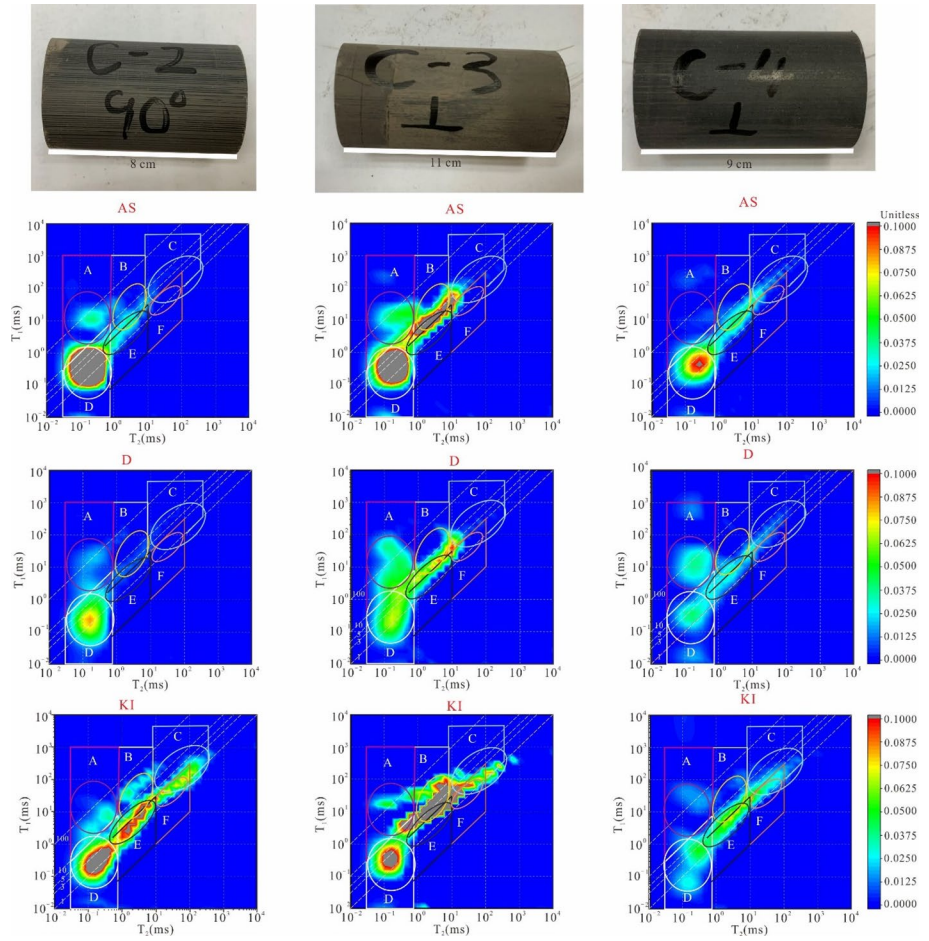

Fig. 8 The T_1–T_2 map and fluid classification on different experimental circumstance in the Cretaceous Qingshankou Formation, Gulong Sag, Songliao Basin

Table 2 The criteria of different fluid types in the Cretaceous Qingshankou Formation, Gulong Sag, Songliao Basin

Regions	Fluid types	T_2 (ms)	T_1/T_2
A	Bitumen, kerogen, and Group OH	< 1	> 10
B	Irreducible oil	1–10	> 3
C	Movable oil	≥ 10	
D	Clay-bound water	< 1	< 10
E	Irreducible water	1–10	< 3
F	Movable water	10–100	< 3

the condition of after being dried at 105 ℃ showed that the signal intensity in the regions B, C, E, and F was weakened (Fig. 8). The signal in the regions C and F representing movable fluid almost completely disappeared. Although the signal in regions B and E was

weakened, the presence of fluid can still be detected (Fig. 8). The reduced signal may be the loss of water in the small pores in the inorganic pores. Some reduced signals are attributed to oil loss because high temperatures would reduce the viscosity and increase the fluidity of oil, which resulted in the discharge of the oil along the connected pores and throats. On the condition of kerosene imbibed, the signal in regions B, C, E, and F of the T_1–T_2 map was significantly enhanced (Fig. 8). The kerosene firstly injected into the large pores and throats and then entered the micropores and small pores. Generally, kerosene cannot flow into intercrystalline pores. However, due to the adsorption of clay minerals, part of the kerosene was attached to the surface of mineral particles or between layers (Zhang et al. 2020; Xi et al. 2023). Therefore, the signal in the region B was enhanced. Obvious fractures (high-angle fractures and lamellation fractures) can be observed in sample C3 (Fig. 8). The T_1–T_2 map of C3 on the condition of after being dried at 105 ℃ exhibited that the signal intensity in regions B, C, and E was significantly weakened, indicating that the development of fractures greatly improves the petrophysical properties of reservoirs and enhances the connectivity between pores and throats, especially for reservoirs without large pores (Fig. 8). The occurrence of fractures has a significant positive effect on fluid migration and discharge in small pores.

4.2.2 Different Fluid Proportion Calculation

According to the classification criteria of six fluid types, the incremental porosity data under T_1–T_2 obtained by two-dimensional nuclear magnetic resonance experiments were used to determine the proportion of different fluid types. The results showed that on the condition of AS, the contents of A (bitumen and solid-like organic matter), B (bound oil), C (movable oil), D (clay-bound water), E (irreducible water), and F (movable water) ranged from 0.09–0.48, 0.02–0.26, 0.01–0.08, 0.23–0.85, 0.04–0.11, and 0.00–0.01, with averages of 0.21, 0.12, 0.03, 0.59, 0.06, and 0.001, respectively (Table 3). On the state of being dried at 105 ℃, the signal percentages A, B, C, D, E, and F variated from that of on the condition of AS, with contents ranging from 0.19–0.54, 0.04–0.24, 0.01–0.08, 0.19–0.70, 0.01–0.10, and 0.00–0.01, with averages of 0.35, 0.11, 0.04, 0.46, 0.05, 0.001, respectively (Table 3). On the condition of kerosene imbibed, the contents of A, B, C, D, E, and F ranged from 0.06–0.50, 0.05–0.41, 0.02–0.09, 0.26–0.70, 0.01–0.30, and 0.00–0.09, with averages of 0.23, 0.15, 0.05, 0.40, 0.12, 0.05, respectively (Table 3). The little change of content of A under different conditions indicated that the properties of bitumen and solid-like organic matter were natural and these environments had no effect on them. This fluid type (bitumen and solid-like organic matter) was mainly enriched in micro and nano pores such as organic matter pores. Notably, higher temperature (more than 110 ℃) could change the structure and molecular composition of clay minerals (Ma et al. 2020). The content of D and E ranged from 0.25–0.88 (with an average of 0.65), from 0.21–0.72 (with an average of 0.50), and from 0.32–0.72 (with an average of 0.52), under the conditions of AS, D, and KI, respectively (Table 3). The content variation indicated that only a little irreducible water was volatile during heating. The content of movable water and movable oil was almost unchanged from conditions AS to D. On the condition of KI, the content of these fluid types variated a lot implying there were large pores and connectivity pores and throats in these rocks. Movable oil filled these reservoir spaces underground. After coring, movable oil was lost along the connectivity pore structure. With the injection of kerosene, fluid was reaccumulated in these spaces. Then, signals could be detected in these regions (Fig. 8, Table 3).

Table 3 The content of different fluid types interpreted through T_1–T_2 map in the Cretaceous Qingshankou Formation, Gulong Sag, Songliao Basin

Fluid types	Conditions	A	B	C	D	E	F
C2	AS	0.11	0.04	0.02	0.79	0.04	0.00
C3	AS	0.14	0.17	0.05	0.56	0.07	0.01
C4	AS	0.09	0.09	0.08	0.61	0.11	0.01
C6	AS	0.10	0.08	0.04	0.69	0.08	0.01
C8	AS	0.09	0.02	0.01	0.85	0.02	0.00
C9	AS	0.15	0.16	0.02	0.57	0.09	0.00
D1	AS	0.40	0.14	0.01	0.43	0.02	0.00
D2	AS	0.48	0.26	0.01	0.23	0.01	0.00
D3	AS	0.27	0.11	0.01	0.56	0.04	0.00
Minimum		0.089	0.024	0.007	0.234	0.014	0.000
Average		0.205	0.119	0.027	0.589	0.056	0.004
Maximum		0.479	0.262	0.077	0.851	0.114	0.011
C2	D	0.19	0.05	0.03	0.70	0.02	0.00
C3	D	0.27	0.15	0.07	0.43	0.07	0.01
C4	D	0.33	0.10	0.08	0.37	0.10	0.01
C6	D	0.35	0.07	0.05	0.47	0.05	0.00
C8	D	0.33	0.04	0.02	0.60	0.00	0.00
C9	D	0.26	0.15	0.03	0.46	0.09	0.00
D1	D	0.49	0.11	0.01	0.36	0.02	0.00
D2	D	0.54	0.24	0.01	0.19	0.02	0.00
D3	D	0.36	0.09	0.02	0.50	0.03	0.00
Minimum		0.194	0.041	0.010	0.189	0.005	0.000
Average		0.347	0.112	0.036	0.455	0.046	0.004
Maximum		0.544	0.240	0.080	0.703	0.097	0.014
C2	KI	0.19	0.05	0.03	0.70	0.02	0.00
C3	KI	0.06	0.41	0.09	0.28	0.09	0.07
C4	KI	0.13	0.15	0.09	0.35	0.19	0.09
C6	KI	0.11	0.17	0.09	0.29	0.26	0.08
C8	KI	0.12	0.10	0.04	0.52	0.16	0.06
C9	KI	0.10	0.19	0.04	0.32	0.30	0.05
D1	KI	0.50	0.07	0.03	0.37	0.02	0.01
D2	KI	0.50	0.13	0.02	0.26	0.05	0.04
D3	KI	0.35	0.09	0.04	0.48	0.02	0.03
Minimum		0.063	0.052	0.020	0.264	0.015	0.004
Average		0.230	0.149	0.054	0.397	0.123	0.047
Maximum		0.503	0.409	0.094	0.703	0.299	0.088

A, the proportion of Bitumen-kerogen-Group OH (unitless). B, the proportion of irreducible oil (unitless). C, the proportion of movable oil (unitless). D, the proportion of clay-bound water (unitless). E, the proportion of Irreducible water (unitless). F, movable water (unitless)

4.2.3 Fluid Identification via 2D NMR Logs

The advanced module of NMR interpretation in Techlog 2019 provides five methods to divide energy clusters, including Expert Mode, Recommended, More Cluster,

Table 4 The classification results of different methods and the best option

Model	Methods numbers	Specific methods	Optimal method	T_1/T_2
Expert Mode	5	Clustering No. 6	Clustering No.6	T_1/T_2_1:6.51
		Clustering No. 2		T_1/T_2 script>_2:5.48
		Clustering No. 3		T_1/T_2 script>_3:0.79
		Clustering No. 4		T_1/T_2 script>_4:2.52
		Clustering No. 5		T_1/T_2 script>_5:8.31
				T_1/T_2 script>_6:0.75
Recommended	9	Clustering No. 8	Clustering No.8	T_1/T_2 script>_1:12.5
		Clustering No. 1		T_1/T_2 script>_2:2.23
		Clustering No. 2		T_1/T_2 script>_3:3.42
		Clustering No. 3		T_1/T_2 script>_4:0.86
		Clustering No. 4		T_1/T_2 script>_5:3.7
		Clustering No. 5		T_1/T_2 script>_6:10.5
		Clustering No. 6		T_1/T_2 script>_7:0.76
		Clustering No. 7		T_1/T_2 script>_8:0.98
		Clustering No. 9		
More Cluster	13	Clustering No. 14	Clustering No.14	T_1/T_2 script>_1:6.44
		Clustering No. 2		T_1/T_2 script>_2:1.84
		Clustering No. 3		T_1/T_2 script>_3:26.6
		Clustering No. 4		T_1/T_2 script>_4:1.98
		Clustering No. 5		T_1/T_2 script>_5:4.83
		Clustering No. 6		T_1/T_2 script>_6:14.2
		Clustering No. 7		T_1/T_2 script>_7:1.59
		Clustering No. 8		T_1/T_2 script>_8:0.65
		Clustering No. 9		T_1/T_2 script>_9:1.24
		Clustering No. 10		T_1/T_2 script>_10:3.14
		Clustering No. 11		T_1/T_2 script>_11:0.61
		Clustering No. 12		T_1/T_2
		Clustering No. 13		script>_12:9.22
				T_1/T_2 script>_13:0.84
				T_1/T_2 script>_14:11.2
Manual Parameter	5	Clustering No. 6	Clustering No.6	T_1/T_2 script>_1:6.51
		Clustering No. 2		T_1/T_2 script>_2:5.48
		Clustering No. 3		T_1/T_2 script>_3:0.79
		Clustering No. 4		T_1/T_2 script>_4:2.52
		Clustering No. 5		T_1/T_2 script>_5:8.31
				T_1/T_2 script>_6:0.75
Difficult Cases	7	Clustering No. 8	Clustering No.8	T_1/T_2 script>_1:1.9
		Clustering No. 2		T_1/T_2 script>_2:6.54
		Clustering No. 3		T_1/T_2 script>_3:2.67
		Clustering No. 4		T_1/T_2 script>_4:0.88
		Clustering No. 5		T_1/T_2 script>_5:3.23
		Clustering No. 6		T_1/T_2 script>_6:0.81
		Clustering No. 7		T_1/T_2 script>_7:7.1
				T_1/T_2 script>_8:1.03

Clustering No.8 means that there are 8 regions (energy clusters) that are classified and T_1 / T_2script>_1:1.9 means the ratio of T_1 to T_2 of the main peak signal in region 1 is of 1.9. In the second track-specific methods, the optimal solution is arranged first, followed by others in numerical order

Manual Parameter, and Difficult Cases (Table 4). Each provides several interpreted results (Table 4, Fig. 9). In the Expert Mode, five interpreted results are obtained. Of all of these, Clustering No.6, in which the method of dividing six energy clusters is the

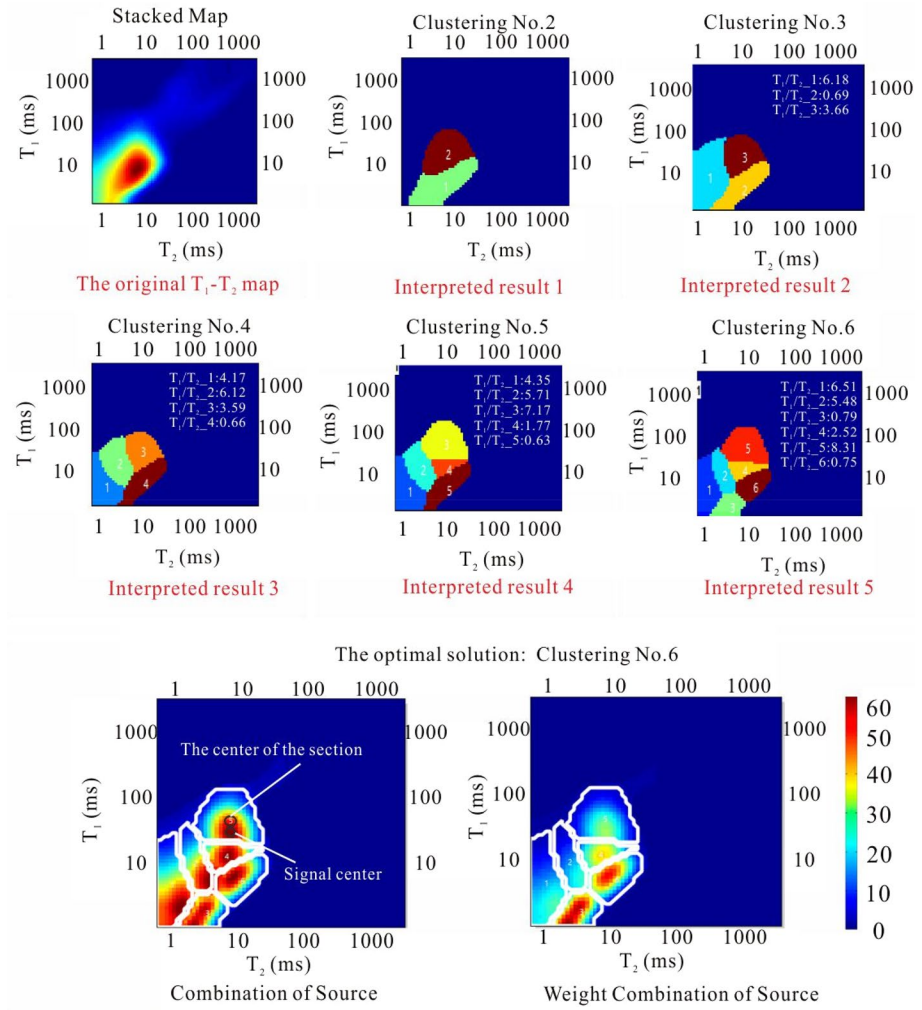

Fig. 9 The modeling of energy cluster interpreted by Expert Mode

best-most of the signal center of every energy cluster is located in the center of each section (Fig. 9).

According to the classification criteria of six fluid types of experimental conditions, the fluid type of each energy cluster in T_1–T_2 maps derived from CMR-NG logging was defined (Fig. 10). Compared with the experimental data, the value ranges of T_1–T_2 recorded in the CMR-NG logging were smaller (Fig. 10). The component OH groups with short relaxation time cannot be detected, nor can solid-like organic matter and kerogen be obtained. The number of energy clusters divided by the optimal classification of each model is not the same, and the signal peak position of each energy cluster is also different. Since the boundary of energy clusters is not exactly consistent with the boundary of fluid types division, it might bias different components in CMR-NG logging. For example, region 5 of the T_1–T_2 map in Fig. 10A is defined as bound oil, but in fact, it

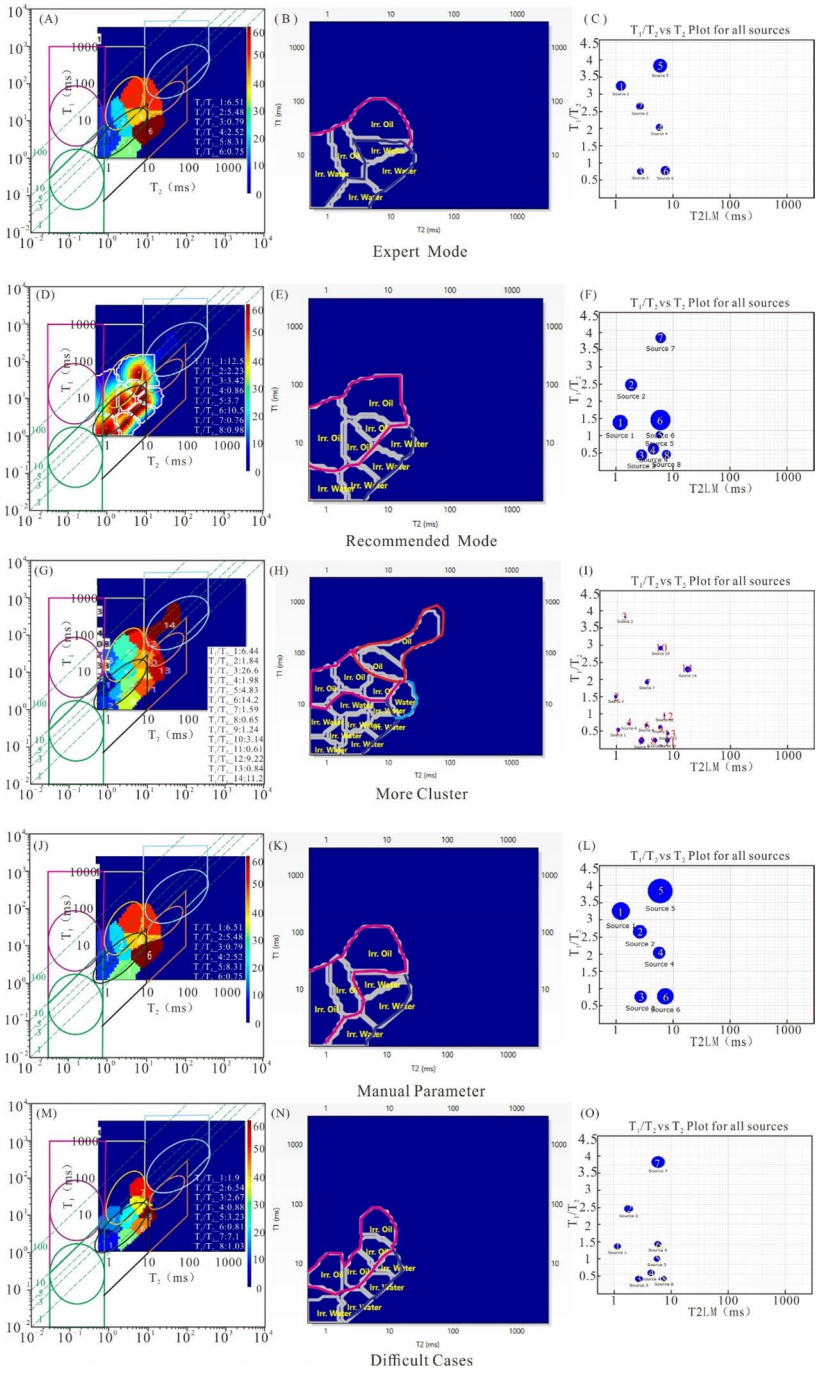

Fig. 10 The criteria of fluid types identified by these five methods in the Qingshankou Formation, Gulong Sag, Songliao Basin (Well 7)

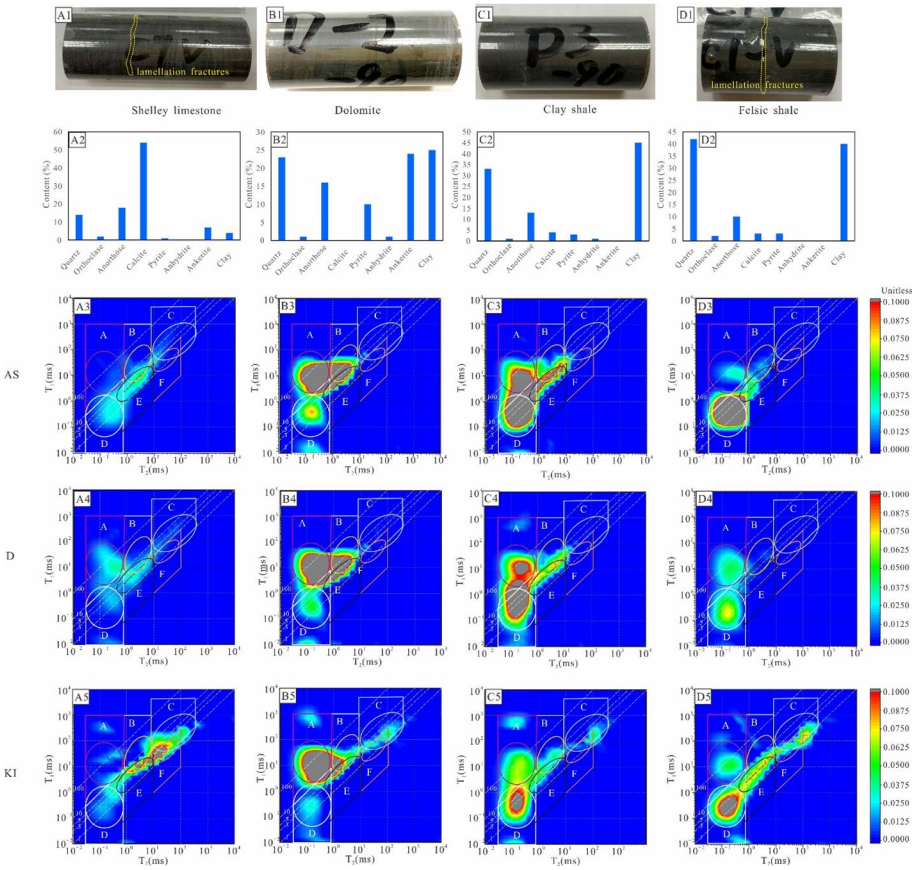

Fig. 11 The features T_1–T_2 map of different lithologies under different experimental conditions in the Cretaceous Qingshankou Formation, Gulong Sag, Songliao Basin

also contains irreducible water. Therefore, there is a certain error in the interpretation of the results of the well log data.

5 Discussion

5.1 T_1–T_2 Maps of Various Lithologies

The two-dimensional NMR spectra of different lithology samples on three conditions (AS, D, and KI) were measured. The results show that the T_1–T_2 maps of different lithologies characterized by different mineral compositions are different.

The C7 sample is a shelly limestone that contains calcite, felsic, and clay minerals in the value of 54%, 34%, and 4%, respectively, with low total organic carbon and sulfur (Fig. 11A$_1$, A$_2$, Table 5). On the condition of the original state (as received), the T_1–T_2 map showed that the main fluid types were *D* (clay-bound water) and E (irreducible water) in small pores (Fig. 11A$_3$) (Li et al. 2018; Khatibi et al. 2019). The signal intensity of

Table 5 The mineral composition and content of four types of lithology in the Qingshankou Formation, Gulong Sag, Songliao Basin

Samples	C7	D2	D3	C1
Quartz (%)	14	23	33	42
Orthoclase (%)	2	1	1	2
Anorthose (%)	18	16	13	10
Calcite (%)	54	0	4	3
Pyrite (%)	1	10	3	3
Siderite (%)	0	0	0	0
Gypsum (%)	0	0	0	0
Anhydrite (%)	0	1	1	0
Ankerite (%)	7	24	0	0
Clay (%)	4	25	45	40
Apatite (%)	0	0	0	0
TOC (%)	0.75	7.98	4.17	2.17
Sulfur (%)	0.18	4.33	1.29	2.14

these two regions was not high. The main peak signal in region *D* was with the T_2 value of 0.4 ms and T_1 / T_2 value of 2 (Fig. 11A3). The main peak signal in region E was located at T_2 value of 2 ms and $T1$ / T_2 of 3 (Fig. 11A3). After being dried, the signals in both regions were weakened (Fig11A4). After the samples were saturated with kerosene at normal temperature, the signals in regions B and C were significantly enhanced, which may be attributed to the development of lamellation fractures resulting in the injection of kerosene into the rock along the fractures (Fig. 11A1, A5).

Sample D2 was defined as dolomite consisting of ankerite, clay minerals, and felsic with the values of 24%, 25%, and 40%, respectively (Fig. 11B1, B2 Table 5). As received state, the T_1 / T_2 displayed that the fluid types of multi-porous media were mainly A, B, D, and E, that were, bitumen, clay-bound water, irreducible water, and immovable oil (Fig. 11B3). The values of T_2 and T_1 / T_2 of the main peak signal were 0.2 ms and 40 in region A (Fig. 11B3). The high ratio of longitudinal to transverse relaxation time indicated that the content of macromolecular compounds in solid organic matter increased. The main peak signal of region D is located at T_2 of 0.2 ms and T_1 / T_2 of 3 (Fig. 11B3). The signal in this region is significantly weaker than that in other regions. The signal in region B was concentrated at T_2 value of 2 ms with the value T_1 / T_2 of 7, indicating mainly bound oil in micropores and small pores. On the condition after being dried at 105 ℃, the signal in D region was weakened because of some water evaporating, whereas the signal in regions B and E had no obvious change (Fig. 11B4). On the condition of kerosene imbibed, the signal in region C was enhanced after the kerosene first entering the larger connecting pores (Fig. 11B5).

Sample D3 mainly contained clay minerals, felsic, and calcite felsic with the value of 45%, 47%, and 4%, respectively, which was a clayed shale (Fig. 11C1,C2, Table 5). As received state, T_1–T_2 map, the main peak signal in region A was located at T_2 value of 0.2 ms and the ratio of T_1–T_2 being 30 (Fig. 11C3). The main peak signal in region D was at T_2 value of 0.2 ms and T_1 / T_2 of 3. The signals in regions B and E cannot be separated accurately, which was concentrated in the T_2 ranging from 1 ms to 10 ms and T_1 / T_2 ranging from 2 to 10 (Fig. 11C3). The dominant fluid type of regions B and E was bound oil (irreducible oil). After beingdried, the signal in regions A, B and E of the T_1–T_2 map was weakened (Fig. 11C4). The decreased signal intensity in region A may be attributed to the rising temperature. Higher temperature contributes to the composition changes of organic matter, the decreasing viscosity of

the polymer and the macromolecular compound. All of these reactions can result in a decrease in T_1. After the kerosene was imbibed, a new signal in region C appeared, indicating that there were a small number of large inorganic pores in the rock (Fig. 11C5). Movable oil stored in these pores before was lost during the process of drilling coring. Therefore, this component cannot be detected on the condition of AS.

The main mineral composition in Sample C1 was clay, felsic, and shale with the value of 40%, 54%, and 3%, respectively (Fig. 11 D1, D2, Table 5). This sample was defined as felsic shale. The signal intensity in region A was low, whereas the signal in region D was strong with the main peak located at the T_2 value of 0.2 ms and T_1/T_2 value of 3 (Fig. 11D3). The main fluid type of this sample was clay-bound water. After being dried at 105 ℃, the signal intensity in region D decreased significantly, and the weak signal in region E completely disappeared (Fig. 11 D4). On the condition of kerosene imbibed, the signals in all six regions are significantly enhanced, which is attributed to the adsorption of clay minerals (Fig. 11 D5). In the process of kerosene injection, kerosene is absorbed by clay minerals and then attached to the surface of particles and interlayers (Zhang et al. 2020; Xi et al. 2023). Therefore, signals can be detected in different pore sizes.

The response characteristics of the above four samples representing four types of lithologies are different on T_1–T_2 maps. On the condition of AS, compared with the other three types, the shelly limestone (sample C7) displayed almost no signal in regions A and B with T_2 less than 1 ms (Fig. 11A3). However, the clay-prone shale (D2), dolomite (D3) and felsic shale (C1) showed stronger signals in these regions, indicating more organic carbon hosted in shales (Fig. 11B3, C3, D3). Compared with clay-prone shale, the T_1–T_2map of felsic shale sample showed the signal intensity of region A (solid-like organic matter) was significantly weakened, indicating that organic matter in felsic shale has a high degree of transformation or the oil mainly came from near-source oil rather than in-situ (Fig. 11A, D) (Liu et al. 2018; Gao et al. 2022; He et al. 2022). However, the hydrocarbons in clay-prone shale were mainly in-situ oil and gas (oil generation and storage in the same area). After the saturation of kerosene, the signals in regions B, C, E, and F in felsic shale and shelly limestone were significantly strengthened (Fig. 11A5, D5). This was mainly because the development of lamellation fractures greatly improved the petrophysical properties and enhanced the connectivity of pores and throats of the reservoir (Fig. 11A, D).

5.2 Contribution of Organic Matter and Mineral Composition

To investigate the factors controlling and accumulation status of multi-porous media fluid types, relationships between the content of each fluid type and pyrolysis parameters and mineral components content were established. Correlation coefficients square (R^2), defined for NMR signal of native-state samples (as received) from regions A–F and TOC, S_1, S_2, Pg, CO_2, S_3, and S_4, was summarized. For further analysis, the threshold of R was defined as 0.7 (Mukhametdinova et al. 2021). Therefore, when R^2 is greater than 0.49, the correlation between two parameters is good, which is highlighted in bold (Tables 6-8). The correlation between TOC content and hydrocarbon generation potential is not always positive. Some source rocks contain high TOC content but show poor hydrocarbon generation potential. Because TOC is mostly provided by ineffective carbon and these carbon compounds hardly contribute to hydrocarbon generation in these rocks (Hu et al. 2021). The cross-plot of TOC and Rock–Eval pyrolysis parameters showed that the TOC content of Qingshankou Formation in the Gulong Sag was positively correlated with the potential of hydrocarbon generation, but was relatively weakly

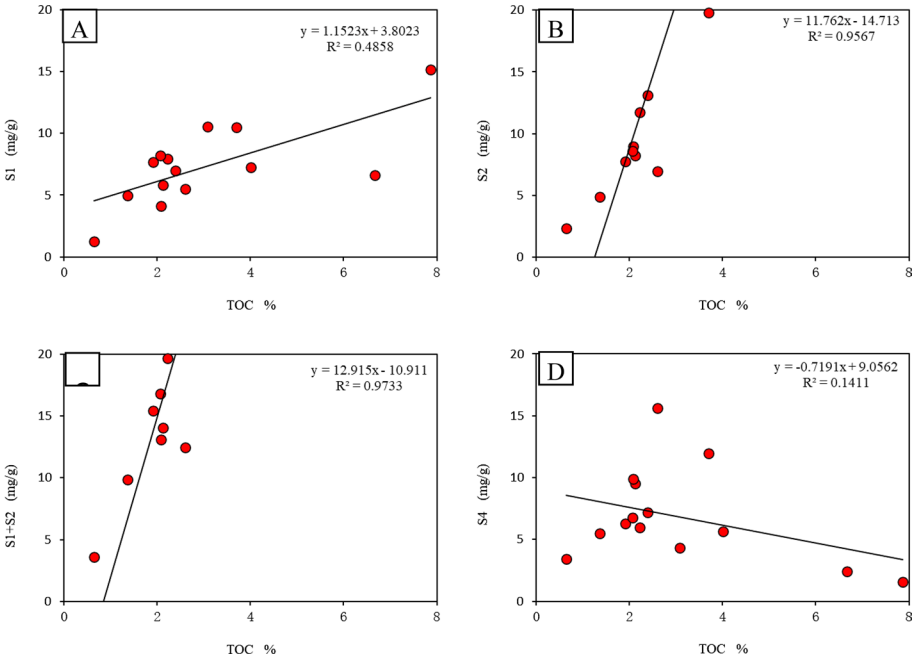

Fig. 12 Cross-plot of TOC and rock pyrolysis parameters in the Qingshankou Formation, Gulong Sag, Songliao Basin

Table 6 The relationship between fluid types and geochemistry parameters on the condition of original state

R^2	A	B	C	D	E	F
TOC(%)	**(+) 0.9442**	**(+) 0.6245**	(−) 0.2527	**(−) 0.7813**	(−) 0.3731	(−) 0.2131
S_1(mg/g)	(+) 0.3228	**(+) 0.7867**	(−) 0.0308	**(−) 0.5430**	(−) 0.0310	(−) 0.0134
S_2(mg/g)	**(+) 0.9765**	**(+) 0.5390**	(−) 0.2770	**(−) 0.7598**	(−) 0.3759	(−) 0.2543
S_1+S_2(mg/g)	**(+) 0.9695**	**(+) 0.6159**	(−) 0.2599	**(−) 0.8020**	(−) 0.3489	(−) 0.2328
S_3(mg/g)	(+) 0.0001	(+) 0.1829	(+) 0.0341	(−) 0.0701	(+) 0.1564	(+) 0.0705
S_4(mg/g)	**(−) 0.5191**	(−) 1.2193	(+) 0.1411	(+) 0.4196	(+) 0.0598	(+) 0.2030

Caption: + represents positive correlation,− means negative correlation

correlated with the content of soluble hydrocarbons (free hydrocarbons), and had nothing to do with residual hydrocarbons (Fig. 12).

As received (AR): the most significant correlations are for region A (bitumen, kerogen, and group OH) versus TOC, S_2, and Pg (hydrocarbon generation potential) regions; region B (bound oil) versus TOC, S_1, S_2, and Pg (Table 6, Fig. 13A,B). According to the value of R^2, component A is controlled by S_2 and B is mostly affected by S_1. A strong positive correlation between region D (irreducible water) and TOC, S_1, S_2, and Pg is displayed, indicating that when organic matter or oil and gas are enriched in the rocks, the pores are mostly enriched with hydrocarbon components.

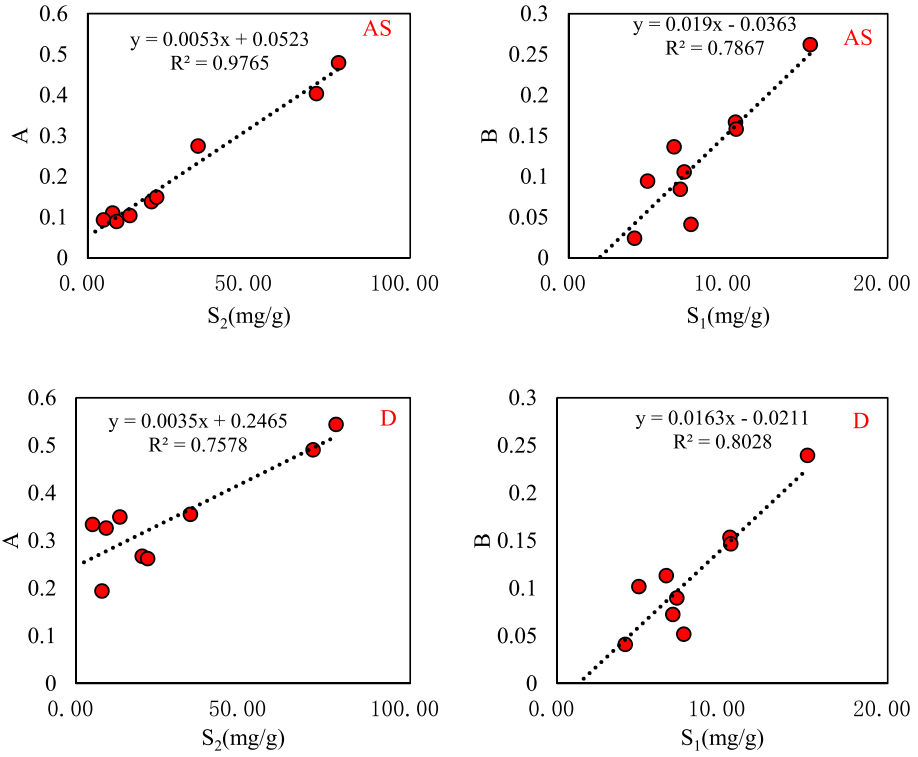

Fig. 13 Cross-plot of A and B versus rock pyrolysis parameters at the native and dried states

After being dried at 105 ℃ (D): the value of R^2 is lower than that of the original state, implying a weaker correlation between pyrolysis parameters and regions A, B, and D (Table 7, Fig. 13C, D). Region A (bitumen, kerogen, and group OH) shows a strong positive correlation with S_2, followed by Pg, and then TOC content. There is a strong relationship between Region B (bound oil) and S_1. Similar to the original state, there is a good negative correlation between region D and the pyrolysis parameters (Table 7).

Kerosene imbibed (KI): the correlation between different fluid types and geochemical parameters is very weak. Only region A (bitumen, kerogen, and group OH) has a good positive correlation with S_2, Pg, and TOC (Table 8). No matter what condition it is, region A shows a good relationship with S_2 (Tables 6, 7, 8). This may be explained by the stable properties of component A. At the dried state, some water in components B (bound oil) and E (irreducible water) is lost due to high temperature. Notably, water signals can be captured at the border of regions B and E. At the saturated kerosene state, kerosene and hydrocarbon enriched in rocks will dissolve together due to their similar chemical properties (the same polarization), as well as the absorption of clay minerals and organic on kerosene (Zhang et al. 2020; Xi et al. 2023).

Although the principle of NMR experiment is the interaction between the spin nuclei and the external magnetic field and the rock matrix has little influence (Lai et al. 2018; Khatibi et al. 2019). Previous studies have found that some mineral components such as clay minerals and quartz may affect the results of nuclear magnetic measurement (Hu

Table 7 The relationship between fluid types and geochemistry parameters on the condition of dried state

R^2	A	B	C	D	E	F
TOC (%)	**(+) 0.6958**	**(+) 0.5456**	(−) 0.3761	**(−) 0.5137**	(−) 0.145	(−) 0.3631
S_1 (mg/g)	(+) 0.1046	**(+) 0.8028**	(−) 0.0564	(−) 0.3279	(+) 0.0004	(−) 0.0988
S_2 (mg/g)	**(+) 0.7578**	(+) 0.4596	(−) 0.4270	***(−) 0.5050***	(−) 0.1551	(−) 0.3800
Pg (mg/g)	**(+) 0.7175**	**(+) 0.5381**	(−) 0.4035	**(−) 0.5284**	(−) 0.1325	(−) 0.3716
S_3 (mg/g)	(+) 0.0178	(+) 0.2052	(+) 0.0077	(−) 0.1777	(+) 0.2206	(+) 0.0061
S_4 (mg/g)	(−) 0.3993	(−) 0.1914	(+) 0.3100	(+) 0.2693	(+) 0.0146	(+) 0.1933

Table 8 The relationship between fluid types and rock pyrolysis parameters at kerosene imbibed state

R^2	A	B	C	D	E	F
TOC(%)	**(+) 0.7407**	(−) 0.0060	(−) 0.2661	(−) 0.1703	(−) 0.2413	(−) 0.1850
S_1(mg/g)	(+) 0.1087	(+) 0.1048	(−) 0.0793	(−) 0.2088	(−) 0.0151	(−) 0.0198
S_2(mg/g)	**(+) 0.8364**	(−) 0.0415	(−) 0.3081	(−) 0.1360	(−) 0.2410	(−) 0.2155
S_1+S_2(mg/g)	**(+) 0.7899**	(−) 0.0232	(−) 0.3012	(−) 0.1565	(−) 0.2218	(−) 0.2007
S_3(mg/g)	(−) 0.0460	(+) 0.0800	(+) 0.0218	(−) 0.3644	(+) 0.4403	(+) 0.3543
S_4(mg/g)	(−) **0.5792**	(+) 0.3655	(+) 0.3306	(+) 0.0195	(+) 0.0276	(+) 0.1671

Table 9 The relationship between fluid types and mineral contents at the original, dried, and kerosene saturation states

R^2	A	B	C	D	E	F
As received						
Clay %	0.0215	0.2006	0.1125	0.0754	0.0030	
Felsic %	0.1644	0.3558	0.0431	0.2774	0.0005	0.0003
Carbonate %	0.0306	0.2283		0.1411	0.0735	0.0008
Sulfur %	0.4184	0.2538	0.3193	0.2778	0.2391	0.4154
After being dried at 105 °C						
Clay %	0.0037	0.2096	0.0351	0.0984	0.1802	0.0072
Felsic %	0.0155	0.3881	0.1100	0.1173	0.0046	0.0072
Carbonate %	0.0011	0.2701	0.0206	0.1023	0.1795	0.0004
Sulfur %	0.2996	0.2855	0.4704	0.1684	0.1365	0.2785
Kerosene imbibed						
Clay %		0.0019	0.0811	0.1077	0.2780	0.0034
Felsic %	0.0842	0.0131	0.2611	0.0258	0.0073	0.0034
Carbonate %	0.0026	0.0034	0.0947	0.0677	0.1679	0.0004
Sulfur %	0.3725	0.2389	0.5990	0.0027	0.0113	0.1583

et al. 2021; Mukhametdinova et al. 2021; Wu et al. 2021). In addition, Mukhametdinova's study shows that clay mineral content has a strong correlation with structural water at dried state. At water-saturated state, quartz content has a good correlation with bitumen, bound oil and mobile oil and quartz content has a good correlation with macropores and fluid enriched in macropores (Mukhametdinova et al. 2021). The main mineral

components in this study are quartz, feldspar, and clay minerals. For better analysis of the factors controlling of different fluid types, relationships between various mineral contents and different fluid contents are established. Table 9 shows the value of R^2 between different fluid types and rock mineral compositions under three states. The results show that there is no obvious relationship between fluid types and the content of various minerals.

5.3 Distribution of Fluid Saturation in a Single Well

Among these five methods, Expert Mode and Manual Parameter models had completely consistent interpretation results (Fig. 10). Five methods were provided and the optimal solutions were the one that divided the signal into six regions. The peak signals in each region were the same as well. The Recommended model and the Difficult case model have the same explanatory conclusions, but their explanatory processes are slightly different. The Recommended model provides 9 methods, among which the scheme divided the signal into 8 regions is the best. The Difficult case model provides 7 methods and the method divided into 8 regions is the most reasonable. Although the favorable method is to classify the signal into 8 regions in both models, the parameter values of each region are slightly different. The interpretation of the results of the More Cluster model is quite different from that of the other four models. As more regions are divided, more information can be extracted. Figure 10G shows that signal appeared in a long relaxation time (larger than 10 ms) indicating movable fluid components (movable oil and water). Due to the lack of oil saturation data measured by experiment, oil tests and production data were used to determine and validate the optimal model. The oil test results showed that the output of well GY7 was low (Fig. 14). The calculated result of the Expert Mode model showed the closest interpretation to the oil test. Therefore, the Expert Mode model was selected to calculate the fluid saturation in the subsequent evaluation process.

Logging evaluation of fluid saturation can be identified by Expert Mode model. It should be noted that bound oil, irreducible water, mobile oil, and mobile water cannot be completely separated due to the limitations of experimental conditions and accuracy and the complexity of fluids composition. The T_1–T_2 responses of different fluids have a certain overlap. Therefore, there are some deviations in the calculation results of fluid saturation using CMR-NG logging calibrated by experiment. Figure 15 shows the calculation results that bound oil and irreducible water are the dominant fluids of the Qingshankou Formation in GY 7. The frequency distribution histograms of bound oil and irreducible water saturation in each stratum from Q1 to Q9 are shown in Fig. 15. The variation of bound oil saturation and irreducible water saturation in six strata (Q1–Q5 and Q7) is slight. The bound oil saturation ranges from 30 to 60%, and the irreducible water saturation ranges from 40 to 70%. On the contrary, in strata Q6, Q8, and Q9, water and oil saturation change quickly. The average irreducible water saturation is about 46%, which is slightly higher than the bound oil saturation of about 54%.

6 Summary and Conclusions

The first member and lowermost part of the second member of the Cretaceous Qingshankou Formation, which is characterized by high TOC content with an average value of 3.46%, is present within the Gulong Sag, Songliao Basin located in northeastern China.

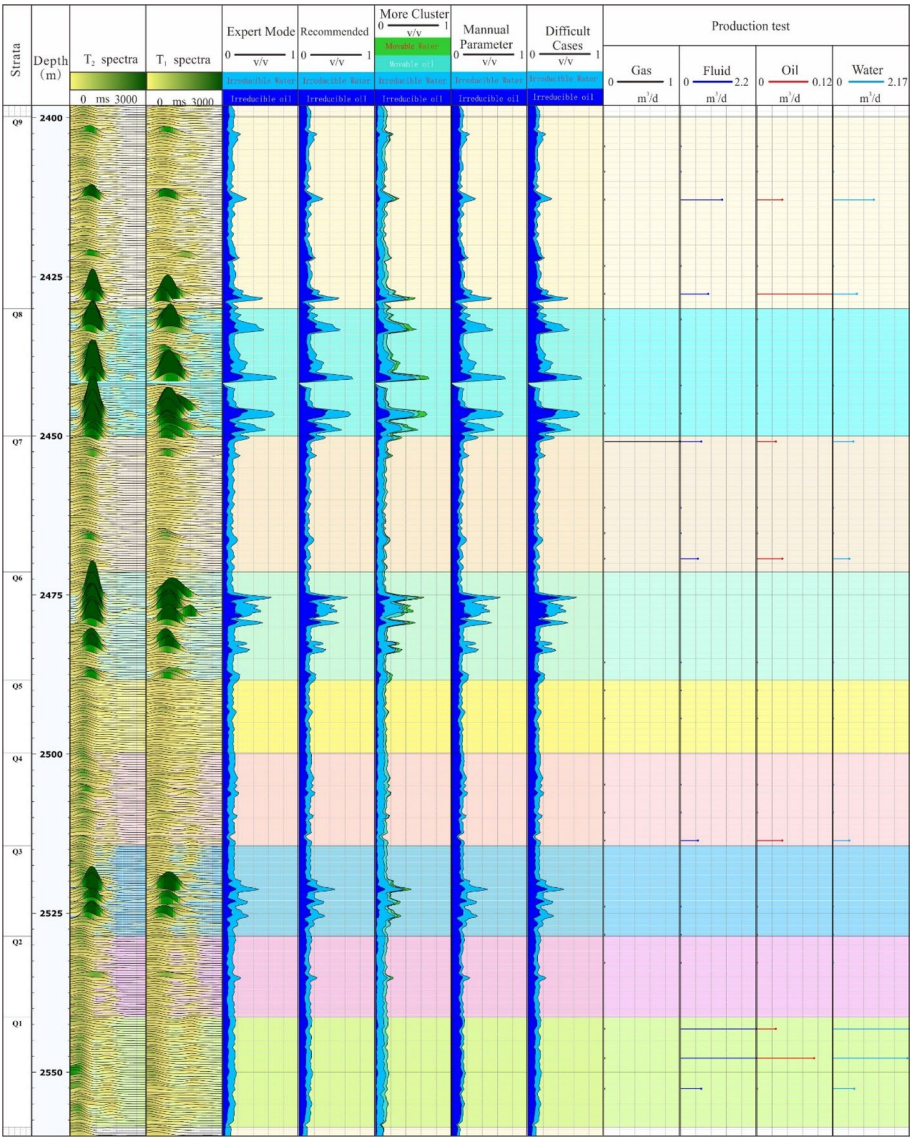

Fig. 14 The content of different fluid types calculated by these five methods in the Qingshankou Formation Gulong Sag, Songliao Basin (Well 7)

Parameters (I_H, I_O, T_{max}, and R_o) obtained from Rock–Eval pyrolysis analyses illustrate the presence of kerogen of types I and II, implying that the source rocks are in the main stage of oil generation.

Five types of lithologies were identified. The dominant lithologies are clay-prone shales and felsic shales, which together account for 80%. With the development of algae and burial history evolution (compaction and cementation), the shale in the Qingshankou Formation of the Gulong Sag was featured with abundant laminae (beddings) and lamellation

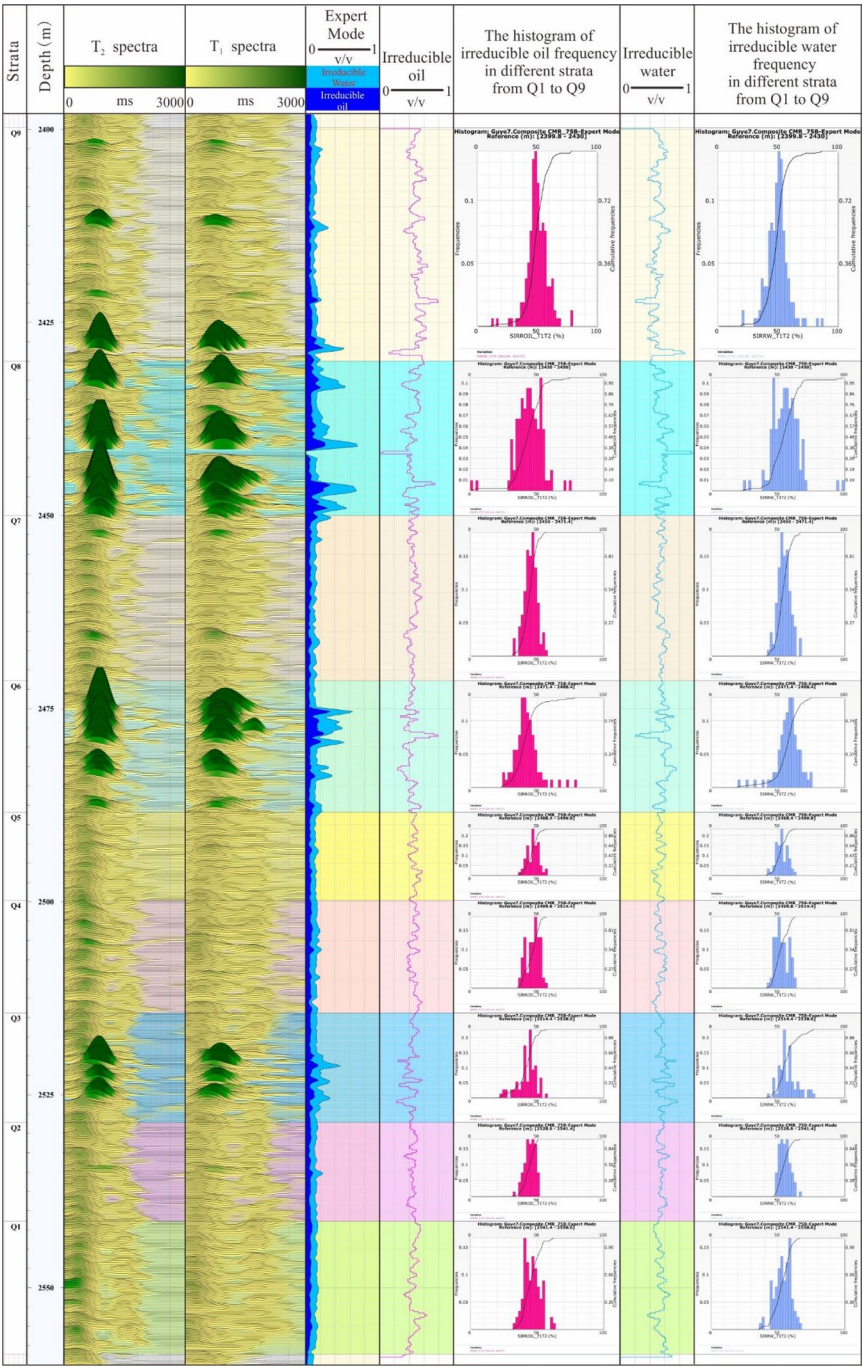

Fig. 15 The fluid saturation calculated by Expert Mode in a single well in the Qingshankou Formation, Gulong Sag, Songliao Basin (Well 7)

fractures. The main reservoir spaces were organic matter pores, intercrystalline pores, intraparticle dissolution pores, and lamellation fractures.

According to the value of T_2 and the ratio of T_1–T_2 obtained from 2D NMR experiment, six fluid types were classified, including kerogen-bitumen-Group OH, irreducible oil, movable oil, clay-bound water, irreducible water, and movable water. Due to the resolution limitation of CMR-NG, the signal of kerogen-bitumen-Group OH and clay-bound water cannot be detected; therefore, only four fluid types can be identified. Among the five models of fluid interpretation conducted by Techlog 2019, Clustering No. 6 in Expert Mode was proposed as being the most favorable method for logging evaluation of fluid types. The contents of bitumen and irreducible oil are controlled by S_2 and S_1, respectively, with no response to the mineral composition. The main fluid was irreducible oil and water in the Qingshankou Formation in GY 7. Strata Q8–Q9 were selected as the highly prospective shale oil reservoirs.

Acknowledgements This work is financially supported by the National Natural Science Foundation of China (Grant No. 42002133), 2022 AAPG Foundation Grants-in-Aid Program, and Science Foundation of China University of Petroleum, Beijing (No. 2462024XKBH009). The authors would like to express their sincere thanks to the PetroChina Daqing Company and PetroChina Research Institute of Petroleum Exploration and Development for their assistance in providing the data, and for their technical input to this work. My joint doctoral studies were funded by China Scholarship Council for one year. I am profoundly indebted to this. I am most grateful for this. We also thank the Editor in Chief and the reviewers for providing excellent advice on the manuscript.

References

Ballinas MR, Bedle H, Devegowda D (2023) Supervised machine learning for discriminating fluid saturation and presence in subsurface reservoirs. J Appl Geophys 217:105192

Baowen CUI, Zhang S, Xiuli FU (2021) Organic sequence stratigraphic division and its influencing factors' analyses for gulong shale in songliao basin. Petrol Geol Oilfield Dev Daqing 40(5):13–28

Cheng YH (2019) Sedimentary filling and tectonic thermal events since Late Cretaceous in the Songliao Basin. China Univ, Geosci

Du JX (2015) Characteristics of gravity flow sediment and its geologic significance in northern songliao basin. Acta Sedimentol Sin 33(2):385–393

EIA (2023) Annual energy outlook 2023.

Fang Y, Zhang WY, Ma F, Cheng L, Shi F (2019) Research on the global distribution and development status of shale oil. Conserv Util Miner Resour 39(5):126–134

Feng Z, Liu B, Shao HM, Wang C, Hong SX, Wang JP, Pan HF, Wang YC, Zhang AD, Tian SS, Chi YA (2020) The diagenesis evolution and accumulating performance of the mud shale in qingshankou formation in gulong area, songliao basin. Petrol Geol Oilfield Dev Daqing 39(3):72–85

Feng Z, Huo Q, Zeng H, Wang YZ, Jia YS (2021) Organic matter compositions and organic pore evolution in gulong shale of songliao basin. Petrol Geol Oilfield Dev Daqing 40(5):40–55

Fleury M, Maria Romero-Sarmiento (2016) Characterization of shales using T_1–T_2 NMR maps. J Petrol Sci Eng 137:55–62

Fu X, Zhang S, Wang H et al (2014) Sedimentary characteristics of the gravity flow reservoirs in qingshankou formation of gulong. Area 33(5):56–62

Gao B, He W, Feng Z, Shao H, Zhang A, Pan H, Chen G (2022) Lithology, physical property, oil-bearing property and their controlling factors of gulong shale in songliao basin. Petrol Geol Oilfield Dev Daqing 41(3):68–79

Ge RF, Zhang QL, Wang LS, Xie GA, Xu SY, Chen J, Wang XY (2010) Tectonic evolution of songliao basin and the prominent tectonic regimetransition in eastern China. Geol Rev 26(2):180–195

Guo J, Xie R, Xiao L, Jin G, Gao L (2019) Nuclear magnetic resonance T_1–T_2 inversion with double objective functions. J Magn Reson 308:106562

Han Y, Zhou C, Yu J, Li C, Hu F, Xu H, Yuan C (2019) Experimental investigation on the effect of wettability on rock-electricity response in sandstone reservoirs. Fuel 239:1246–1257

He WY, Cui BW, Wang FL et al (2022) Study on reservoir spaces and oil states of the cretaceous qingshankou formation in gulong sag Songliao Basin. Geol Rev 68(2):693–741 (**in Chinese with English abstract**)
Hu T, Pang X, Jiang F et al (2021) Movable oil content evaluation of lacustrine organic-rich shales: methods and a novel quantitative evaluation model. Earth-Sci Rev 214:103545
Khatibi S, Ostadhassan M, Xie ZH, Gentzis T, Bubach B, Gan Z et al (2019) NMR relaxometry a new approach to detect geochemical properties of organic matter in tight shales. Fuel 235:167–177
Lai J, Wang G, Wang Z, Chen J, Pang X, Wang S, Zhou Z, He Z, Qin Z, Fan X (2018) A review on pore structure characterization in tight sandstones. Earth Sci Rev 177:436–457
Li CL, Yan WL, Wu HL, Tian H, Zheng JD, Yu J, Feng Z, Xu HJ (2022) Calculation of oil saturation in clay-rich shale reservoirs: a case study of qing 1 member of cretaceous qingshankou formation in Gulong Sag, Songliao Basin NE China. Petrol Explor Dev 49(6):1351–1363
Li J, Huang W, Lu S, Wang M, Chen G, Tian W, Guo Z (2018) Nuclear magnetic resonance T_1–T_2 map division method for hydrogen-bearing components in continental shale. Energy Fuel 32:9043–9054
Li M, Ma X, Jiang Q, Li Z, Pang X, Zhang C (2019) Enlightenment from formation conditions and enrichment characteristics of marine shale oil in North America. Petrol Geol Recovery Effic 26(1):13–28
Li S, Zhu X, Li S, Gong C, Pan R, Chen H (2020) Trigger mechanisms of gravity flow deposits in the lower cretaceous lacustrine rift basin of lingshan island East China. Cretac Res 107:104269
Li Z, Lei Z, Shen W et al (2023) A comprehensive review of the oil flow mechanism and numerical simulations in shale oil reservoirs. Energies 16(8):3516
Liang M, Wang Z, Zheng J, Li X, Wang X, Gao Z, Luo H, Li Z, Qian Y (2015) Hydrous pyrolysis of different kerogen types of source rock at high temperature-bulk results and biomarkers. J Pet Sci Eng 125:209–217
Liang C, Xiao LZ, Zhou CC et al (2019) Nuclear magnetic resonance characterizes rock wettability: preliminary experimental results. Chin J Geophys 62(11):4472–4481
Liu Z (2005) Oil–gas accumulation intectonic inversion in north songliao basin. Geol Jiangsu 29(3):143–146
Liu B, Shi J, Fu X, Lyu Y, Sun X, Gong L, Bai Y (2018) Petrological characteristics and shale oil enrichment of lacustrine fine-grained sedimentary system: a case study of organic-rich shale in first member of cretaceous qingshankou formation in gulong sag, songliao basin NE China. Petrol Explor Dev 45(5):884–894
Liu B, Wang HL, Fu XF, Bai YF, Bai LH, Jia MC, He B (2019) Lithofacies and depositional setting of a highly prospective lacustrine shale oil succession from the upper cretaceous qingshankou formation in the gulong sag, northern songliao basin, northeast China. AAPG Bull 103(2):405–432
Liu C, Xu X, Liu K, Bai J, Liu W, Chen S (2020) Pore-scale oil distribution in shales of the qingshankou formation in the changling sag, songliao basin NE China. Marine Petrol Geol 120:104553
Liu B, Jiang XW, Bai LH, Lu RS (2022) Investigation of oil and water migrations in lacustrine oil shales using 20 MHz 2D NMR relaxometry techniques. Petrol Sci 19:1007–1018
Ma Y, Wang H, Wang W et al (2020) The application of nuclear magnetic resonance T_1–T_2 maps in the research of sedimentary organic matter: a case study of early mature shale with type I kerogen. J Petrol Sci Eng 194:107447
Martins CMS, Cerqueira JR, Ribeiro HJPS, Garcia KS, da Silva NN, Queiroz AFDS (2020) Evaluation of thermal effects of intrusive rocks on the kerogen present in the black shales of irati formation (Permian), Paraná Basin, Brazil. J S Am Earth Sci 100:102559
Mukhametdinova A, Habina-Skrzyniarz I, Kazak A, Krzyzak A (2021) NMR relaxometry interpretation of source rock liquid saturation—a holistic approach. Mar Pet Geol 132:105165
Pang X, Wang G, Kuang L et al (2023a) Lamellation fractures in shale oil reservoirs: recognition, prediction and their influence on oil enrichment. Mar Pet Geol 148:106032
Pang X, Wang G, Kuang L et al (2023b) Logging evaluation of lithofacies and their assemblage under the control of sedimentary environment—the qingshankou formation in gulong sag, songliao basin. J Palaeogeogr 25(5):1–20
Peters KE, Cassa MR (1994) Applied source rock geochemistry. In: Magoon LB, Dow WG (eds) The petroleum system from source to trap. American Association of Petroleum Geologists, Tulsa, pp 93–120
Qin Y, Zhang G, Zhang J et al (2021) Study on the influence of magnetic field intensity on T_2–T_1 two-dimensional nuclear magnetic resonance experiment progress in geophysics. Pet Geol Oilfield Dev Daqing 36(5):2082–2089
Qin Y, Zhang G, Luo C et al (2022) Two-dimensional NMR characteristics of Jimsar shale oil reservoir. J Central South Univ (sci Technol) 53(9):3387–3400
Ramia ME, Martín CA (2016) Nuclear magnetic resonance relaxation studies in shale. Appl Magn Reson 47(12):1323–1337
Silletta EV, Vila GS, Domené EA et al (2022) Organic matter detection in shale reservoirs using a novel pulse sequence for T_1–T_2 relaxation maps at 2 MHz. Fuel 312:122863
Tang Z (2015) The Accumulation Research of Lithology and Structural-Lithologic Reservoirs in the Western Slope of the Northern Songliao Basin. Dissertation, Chengdu University of Technology

Wang XD, Wang R, Shi WZ et al (2022) Tectonic characteristics and evolution of typical rift basins in eastern china: a case study in the gudian area, songliao basin. Bulletin of Geol Sci Technol 41(03):85–95
Wu J, Liang C, Yang R, Xie J (2021) The significance of organic matter–mineral associations in different lithofacies in the wufeng and longmaxi shale-gas reservoirs in the Sichuan Basin. Mar Pet Geol 126:104866
Xi K, Zhang Y, Cao Y, Gong J, Li K, Lin M (2023) Control of micro-wettability of pore-throat on shale oil occurrence: a case study of laminated shale of permian lucaogou formation in jimusar sag, junggar basin NW China. Pet Explor Dev 50(2):297–308
Yan WL, Zhang ZQ, Chen LC, Zhao ZW, Wang WJ (2021) New evaluating method of oil saturation in gulong shale based on NMR technique. Pet Geol Oilfield Dev Daqing 40(5):78–86
Yarman CE, Mitchell J (2019) A greedy variational approach for generating sparse T_1–T_2 NMR relaxation time distributions. J Magn Reson 301:94–101
Zhang X, Zhu X, Zhong D, Liang B, Cao B, Yang L (2005) Sedimentary facies and its controlling on subtle oil and gas reservoirs of the dainan formation of paleogene in gaoyou sag, subei basin. J Palaeogeogr 7(2):207–218
Zhang P, Lu S, Li J, Chang X (2020) 1D and 2D Nuclear magnetic resonance (NMR) relaxation behaviors of protons in clay, kerogen and oil-bearing shale rocks. Mar Pet Geol 114:104210
Zhang AD, Wang JP, Wang YC, Hong SX, Tan WL (2021) Reservoir space types and oil occurrence of gulong shale in songliao basin. Pet Geol Oilfield Dev Daqing 40(5):68–77
Zhao X, Yang Z, Liu X et al (2023) Study on the flow characteristics of tight oil reservoirs with linear injection and production for volume-fractured horizontal wells. Phys Fluids 35:063112
Zhu L, Wu S, Zhou X, Cai J (2023) Saturation evaluation for fine-grained sediments. Geosci Front 14:101540
Zou C, Feng Y, Yang Z, Jiang W, Zhang T, Zhang H, Wang X, Zhu J, Wei Q (2023) Fine-grained gravity flow sedimentation and its influence on development of shale oil sweet spot intervals in lacustrine basins in China. Pet Explor Dev 50(5):883–897

Authors and Affiliations

Xiaojiao Pang[1,2,3] · Guiwen Wang[1,2] · Lichun Kuang[1,2] · Jin Lai[1,2] · Nigel P. Mountney[3]

✉ Xiaojiao Pang
xiaojiaopang0829@163.com

✉ Guiwen Wang
wanggw@cup.edu.cn

[1] National Key Laboratory of Petroleum Resources and Engineering, China University of Petroleum (Beijing), Beijing 102249, China

[2] College of Geosciences, China University of Petroleum (Beijing), 18 Fuxue Road, Changping, Beijing 102249, China

[3] School of Earth and Environment, Institute of Applied Geoscience, University of Leeds, Woodhouse, Leeds LS29JT, UK